Monthly Notices of the ROYAL ASTRONOMICAL SOCIETY

MNRAS **531,** 3088–3102 (2024) https://doi.org/10.1093/mnras/stae1311
Advance Access publication 2024 May 21

Radiative transfer of 21-cm line through ionized cavities in an expanding universe

Kinwah Wu [1]★, Qin Han [1]★ and Jennifer Y. H. Chan [2,3,4]★

[1] *Mullard Space Science Laboratory, University College London, Holmbury St Mary, Surrey RH5 6NT, UK*
[2] *Canadian Institute for Theoretical Astrophysics, University of Toronto, 60 St George St, Toronto, ON M5S 3H8, Canada*
[3] *Faculty of Arts and Science, University of Toronto, 100 St George St, Toronto, ON M5S 3G3, Canada*
[4] *Dunlap Institute for Astronomy and Astrophysics, University of Toronto, 50 St George St, Toronto, ON M5S 3H4, Canada*

Accepted 2024 May 17. Received 2024 May 17; in original form 2023 September 26

ABSTRACT

The optical depth parameterization is typically used to study the 21-cm signals associated with the properties of the neutral hydrogen (H I) gas and the ionization morphology during the Epoch of Reionization (EoR), without solving the radiative transfer equation. To assess the uncertainties resulting from this simplification, we conduct explicit radiative transfer calculations using the cosmological 21-cm line radiative transfer (C21LRT) code and examine the imprints of ionization structures on the 21-cm spectrum. We consider a globally averaged reionization history and implement fully ionized cavities (H II bubbles) of diameters d ranging from 0.01 to 10 Mpc at epochs within the emission and the absorption regimes of the 21-cm global signal. The single-ray C21LRT calculations show that the shape of the imprinted spectral features are primarily determined by d and the 21-cm line profile, which is parametrized by the turbulent velocity of the H I gas. It reveals the spectral features tied to the transition from ionized to neutral regions that calculations based on the optical depth parametrization were unable to capture. We also present analytical approximations of the calculated spectral features of the H II bubbles. The multiple-ray calculations show that the apparent shape of an H II bubble (of $d = 5$ Mpc at $z = 8$), because of the finite speed of light, differs depending on whether the bubble's ionization front is stationary or expanding. Our study shows the necessity of properly accounting for the effects of line-continuum interaction, line broadening, and cosmological expansion to correctly predict the EoR 21-cm signals.

Key words: line: formation – radiative transfer – H II regions – intergalactic medium – dark ages, reionization, first stars – radio lines: general.

1. INTRODUCTION

At about 0.3 Myr after the big bang, electrons and protons began to combine to form neutral hydrogen (H I) atoms (Planck Collaboration XVI 2014). This allows the photons to decouple from the charged particles and form the relic radiations which then evolved to become the cosmological microwave background (CMB) observed today. The Universe entered a dark age before the first luminous objects began to form. The ultraviolet (UV) photons from the first stars and the X-rays from the first active galactic nuclei (AGNs) are capable of ionizing H I gas, carving out ionized hydrogen (H II) cavities (see e.g. Loeb & Barkana 2001). As these ionized cavities expand (Furlanetto, Zaldarriaga & Hernquist 2004, Furlanetto, McQuinn & Hernquist 2006a) and merge (Iliev et al. 2006; Robertson et al. 2010), the Universe eventually became almost completely reionized, except in some dense self-shielded regions (see e.g. Chardin, Kulkarni & Haehnelt 2018). This Epoch of Reionization (EoR) is believed to start at $z \sim 14$ and complete at $z \sim 6$ based on observations of high-redshift luminous quasars (Fan, Carilli & Keating 2006; Robertson et al. 2010) and large-scale polarization of the CMB (Planck Collaboration XLVI 2016b; Planck Collaboration XLVII 2016c).

These observational constraints, however, suffer from various shortcomings, making it difficult for us to obtain a detailed history of reionization (see e.g. Natarajan & Yoshida 2014; Mesinger 2016). It can be compensated by observing the 21-cm signals produced during the EoR (Baek et al. 2010; Morales & Wyithe 2010; Pritchard & Loeb 2012; Eide et al. 2018, 2020). The 21-cm signals are generated by the spin-flip of H I atoms in the ground state, and correspond to a frequency of $\nu_{21\mathrm{cm}} = 1.42$ GHz (Hellwig et al. 1970; Essen et al. 1971). Due to the abundance of H I gas of the Universe, we will be able to access the full history of the reionization via the 21-cm signals when we overcome the difficulties in observation and data analysis. Several projects including the Low Frequency Array (LOFAR, Zarka et al. 2012; Mertens et al. 2020), Murchison Widefield Array (MWA, Tingay et al. 2013; Trott et al. 2020), the Hydrogen Epoch of Reionization Array (HERA, DeBoer et al. 2017; HERA Collaboration 2022),

★ E-mail: kinwah.wu@ucl.ac.uk (KW); qin.han.21@ucl.ac.uk (QH); jyhchan@cita.utoronto.ca (JYHC)

and the Square Kilometer Array (SKA, Koopmans et al. 2015) are underway.

Currently, most of the studies focus on simulating luminous sources and their contributions to reionization (Santos et al. 2010; Mesinger, Furlanetto & Cen 2011; Xu et al. 2016; Park et al. 2019; Mangena, Hassan & Santos 2020; Gillet et al. 2021; Doussot & Semelin 2022). The calculation of 21-cm signals is merely analytical post-processing of simulation results based on the optical depth parametrization (Furlanetto, Oh & Briggs 2006b; Pritchard & Loeb 2012). Adopting this parametrization implies that the observed 21-cm signal at $z = 0$ at a specific frequency ν_0 unambiguously reflects the properties of H I gas at redshift $z = \nu_{21\mathrm{cm}}/\nu_0 - 1$ along the line of sight (LoS). Line broadening and radiative transfer effects are not correctly accounted for in this parametrization (see also Chapman & Santos 2019).

To quantify the inaccuracies of the 21-cm signals computed with the optical depth parametrization, we adopt a covariant radiative transfer formalism which does not require various assumptions which were used in the derivation of the 21-cm optical depth. We investigate the spectral features imprinted by ionized cavities on the 21-cm spectra at $z = 0$. As most simulations study reionization on scales larger than galaxies ($\sim$1 kpc) and present the statistical properties of reionization, we do not use their detailed ionization structures. Instead, we construct more generic descriptions for evolving ionized cavities in an expanding Universe which is applicable for all length-scales and various ionizing sources, in Section 2. To facilitate the comparison between the covariant method and the optical depth parametrization method, we use the most simplified fully ionized spherical cavities as input ionization structure and calculate their imprints on the 21-cm spectra at $z = 0$. We use cosmological 21-cm line radiative transfer (C21LRT) code which tracks the 21-cm signal in both frequency and redshift space, and takes full account of cosmological expansion, radiative transfer effects, and possible dynamics and kinetic effects, such as those caused by macroscopic bulk flow and microscopic turbulence (Chan et al. 2023). The C21LRT formulation and the computational set-up of radiative transfer calculations are presented in Section 3. We then analyse the spectral features of fully ionized cavities in the absorption and emission regimes of 21-cm global signals and discuss the implications in Section 4. Finally, we summarize the findings in Section 5.

2. IONIZED CAVITIES AND TIME EVOLUTION

The physics of ionization processes and the dynamic models of ionization-front expansion can be found in Axford (1961) (see also, Newman & Axford 1968; Yorke 1986; Franco et al. 2000). For the purposes of this study, a generic description for the ionization bubbles and their expansion is sufficient. However, we summarize all the physical processes pedagogically for completeness of this paper. We then discuss whether the corresponding physics are incorporated in reionization simulations and the implications for the accuracy of the predicted 21-cm signals.

2.1 Model ionized cavities

We only consider H atoms (H I and H II) in our cavity models and C21LRT calculations without any other species. In the following texts, we use 'H I zone' and 'H II zone' for regions filled with only H I or H II gas, respectively, 'partially ionized zone' for regions with both H I and H II gas, and term 'ionized cavities' refers to more general/realistic ionization structures. The H II zones are assumed to be spherical. Although they would not be spherical in reality, adopting this idealized geometry is sufficient for the purpose of this study, i.e. to demonstrate the development of the 21-cm line propagating through evolving ionized cavities, which are driven by continuing ionization together with cosmological expansion.

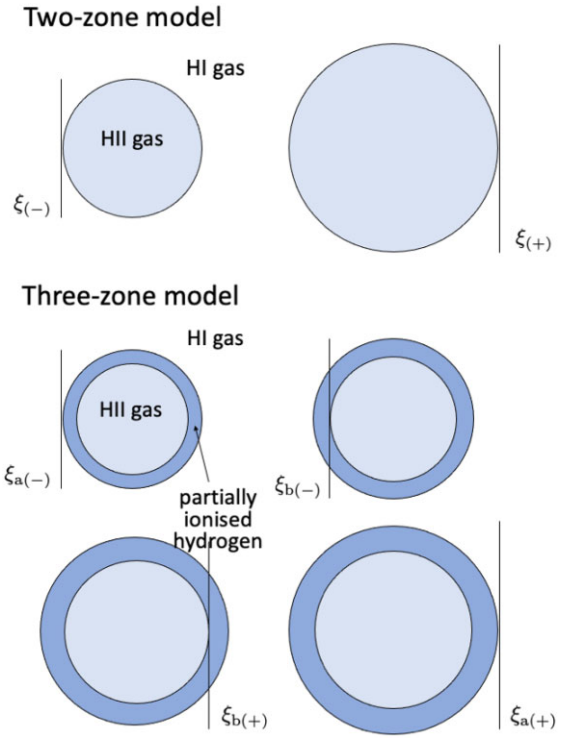

Figure 1. A schematic illustration of the two-zone and the three-zone models. The vertical lines are the locations of the light fronts. In the two-zone model (top row), they are marked by $\xi_{(-)}$ and $\xi_{(+)}$, at the moments when the front reaches and leaves the H II zone, respectively (at $y = 0$). In the three-zone model (middle and bottom rows), they are marked by $\xi_{a(-)}$ and $\xi_{b(-)}$, $\xi_{b(+)}$ and $\xi_{a(+)}$, at the moments when the front reaches the outer boundary of the partially ionized zone, finishes the first passage through the partially ionized zone, starts the second passage through the partially ionized zone, and leaves the partially ionized zone, respectively (at $y = 0$).

For an H II zone surrounded by an infinitely extended H I zone, its size increase are due to (i) photoionization, which is caused by the radiation emitted from the sources embedded inside the H II zone, and (ii) length stretching as a consequence of cosmological expansion. We consider first a two-zone model, which has an insignificant thickness of the transitional interface between the H II zone and the H I zone. We next consider a three-zone model. It has an H II zone surrounded by infinitely extended H I zone, and a layer of partially ionized gas between the H I zone and H II zone. This partially ionized zone has sufficient contribution to the 21-cm line opacity. In this study, we consider that the temperature within each zone is uniform at any instant. Thus, this simplification does not ignore the temperature evolution of the gases in each of the zones.

For both the two-zone and three-zone models, all zones expand only radially. The thickness of the partially ionized zone also increases radially in the three-zone model. To avoid using excessive number of parameters, which may cause unnecessary complications that can mask the physics and the 21-cm line structure, we consider that the partially ionized zone is also uniform at any instant. A schematic illustration of the two-zone and the three-zone models is shown in Fig. 1.

2.2 Ionization induced expansion

We first consider the situation that the time for light traversing the H II zone is negligible compared with the Hubble time. In this situation, cosmological effects can be ignored, and the radiative transfer of the 21-cm line is subject only to the dynamical evolution of the H II zone, which is defined by the propagation of the ionization front. Suppose that the H II zone has a radius r_0 initially. It expands radially at a speed v. The radius of the H II zone at time t is then $r(t) = r_0 + \beta\,\xi(t)$ where $\beta = v/c$, $\xi(t) = c\,t$, and c is the speed of light. Now consider a plane light front propagating in the x-direction (in the Cartesian coordinates) from an initial reference location, x_0. We may set $x_0 = -r_0$. Then the light front will reach $x(t) = -r_0 + \xi(t)$ at time t. It follows that, on the xy-plane, the light front will reach the H II zone boundary at the location (x, y), given by

$$\begin{cases} x = -r_0 + \xi\ ; \\ y = \pm\Big\{ (1+\beta)\xi\ \big[2r_0 - (1-\beta)\xi\,\big]\Big\}^{1/2} . \end{cases} \tag{1}$$

Clearly, at $t = 0$, $(x, y) = (-\,r_0, 0)$. Also, we have

$$\xi_{(\pm)}\Big|_y = \frac{r_0}{(1-\beta)}\left\{1 \pm \left[1 - \left(\frac{1-\beta}{1+\beta}\right)\left(\frac{y}{r_0}\right)^2\right]^{1/2}\right\} , \tag{2}$$

implying that the path that the light front traverses through the H II zone is

$$\Delta\xi\ \Big|_y = \xi_{(+)} - \xi_{(-)} = \frac{2r_0}{(1-\beta)}\ \left[1 - \left(\frac{1-\beta}{1+\beta}\right)\left(\frac{y}{r_0}\right)^2\right]^{1/2} . \tag{3}$$

The time that the light front meets the H II zone boundary for a given y therefore has two values, and they are $t_{(\pm)}|_y = c^{-1}\xi_{(\pm)}|_y$. For a non-expanding H II zone ($\beta = 0$),

$$\Delta\xi\ \Big|_y = 2r_0\ \left[1 - \left(\frac{y}{r_0}\right)^2\right]^{1/2} . \tag{4}$$

This means that expansion leads to LoS length distortion, in terms of a length ratio $\mathcal{R}$:

$$\mathcal{R} = \left(\frac{1}{1-\beta}\right)\left[\frac{1 - \left(\frac{1-\beta}{1+\beta}\right)\left(\frac{y}{r_0}\right)^2}{1 - \left(\frac{y}{r_0}\right)^2}\right]^{1/2} . \tag{5}$$

Note that $\Delta\xi\ |_y = 0$ occurs at

$$y_* = \pm r_0\ \left(\frac{1+\beta}{1-\beta}\right)^{1/2} , \tag{6}$$

instead of at $y = \pm\, r_0$, the values expected for a non-expanding H II zone—it has grown bigger since the light front first intersects the H II zone boundary. Note also that the light path $\Delta\xi$ and hence the light traversing time Δt diverge when $\beta \to 1$ (see equation 3). This corresponds to the situation where the H II zone is expanding so rapidly, in the speed of light, that light propagating from the boundary of one side of the H II zone will never reach the boundary of the other side of the H II zone, as seen by a distant observer.

In the two-zone model, the opacity of the H II zone is provided by the free-electron through Compton scattering. The scattering optical depth of radiation transported across the H II zone at y is

$$\tau_{\rm sc}\ \Big|_y = (n_{\rm e}\,\sigma_{\rm Th})\ \Delta\xi\ \Big|_y , \tag{7}$$

where $n_{\rm e}$ is the electron number density and $\sigma_{\rm Th}$ is the Thompson cross-section. This can be generalized for ionized cavities with any arbitrary opacity κ_ν, at frequency ν, which gives a specific optical depth

$$\tau_\nu\ \Big|_y = \kappa_\nu\ \Delta\xi\ \Big|_y = \frac{2\kappa_\nu r_0}{(1-\beta)}\ \left[1 - \left(\frac{1-\beta}{1+\beta}\right)\left(\frac{y}{r_0}\right)^2\right]^{1/2} , \tag{8}$$

which is in contrast to the specific optical depth expected for a non-expanding cavity:

$$\tau'_\nu\ \Big|_y = 2\kappa_\nu r_0\ \left[1 - \left(\frac{y}{r_0}\right)^2\right]^{1/2} . \tag{9}$$

The remaining question is now how fast the H II zone would expand. We may obtain a rough estimate for the expansion speed v from the following consideration. The boundary of the H II zone advances only when the amount of ionizing radiation is sufficient to convert H I atoms to ions. That is,

$$\beta = \frac{v}{c} \approx \left(1 - \frac{\Upsilon n_{\rm HI}(r)}{n_\gamma(r)}\right) , \tag{10}$$

where n_γ is the number density of ionizing photons, and $n_{\rm H\,I}$ is the number density of H I in the surrounding. The efficiency of converting H I atoms into ions may parametrized by a variable Υ, which is determined by the local atomic and thermodynamic properties (i.e. not the global geometry of the system) and the ratio $(n_{\rm HI}/n_\gamma)$. The expression in equation (10) is essentially a measure of how saturated the ionization process is.

The number density of ionizing photon $n_\gamma(r)$ attenuates with r due to the dilution of radiation over distance and the consumption of the ionizing photons to facilitate the expansion. Thus, the expansion of the H II zone even slows down as ionization approaches saturation, where processes, such as recombination, counteract ionization when the photon supply becomes insufficient. Nonetheless, in the very initial stage when there is a sudden burst of ionizing sources, the supply of n_γ is abundant, and hence the ionization is far from saturation. For $n_\gamma \gg \Upsilon n_{\rm HI}$, the expansion velocity v would be expected to almost reach the speed of light, i.e. $\beta \lesssim 1$. For modest unsaturated ionization, which gives rise a (constant) normalized expansion velocity $\beta = 0.5$, gives $|y_*| = \sqrt{3}\,r_0$, and $\tau_\nu = 4\kappa_\nu r_0 = 2\tau'_\nu$ at $y = 0$ (i.e. radiative transfer along the symmetry axis of the H II zone). Increasing the expansion velocity to $\beta = 0.75$ gives $|y_*| = \sqrt{7}\ r_0$, and $\tau_\nu = 8\kappa_\nu r_0 = 4\tau'_\nu$ at $y = 0$. Here, it shows that ignoring the expansion of H II zone could lead to incorrect inferences for its size and the optical depth.

The situation is slightly more complicated, if there is a partially ionized zone enveloping the H II zone. The partially ionized zone determines the radiative transfer process together with the H II zone. The temperature in the partially ionized zone could be an important variable, especially in the context of radiative transfer of the 21-cm line, as its relative contrast with the temperatures of the background H I gas and the temperature of the H II gas would determine whether a line would appear as emission or as absorption relative to the continuum radiation. Apart from the microscopic aspects, such as radiation processes and radiative transfer, there are subtle issues in the macroscopic perspectives. The inner and outer boundary of the partially ionized zone could expand asynchronously at different speeds. There are also additional issues, which is generally insignificant for the development of the H II zone but might need to be take into account for the development of the partially ionized zone. This is due to the fact that the boundary of the H II zone is an ionization front, not a hydrodynamics shock front, which needs to satisfy certain shock-jump condition, while the interface between the partially ionized zone and the H I zone could be determined by

hydrodynamics and also thermodynamic processes. None the less, we leave the investigation of these subtle yet important physics in a future paper. In this section, we employ a simple parametric model to illustrate how the presence of an additional partially ionized zone would alter the radiative transfer process.

Assume that the H II zone and the partially ionized zone expand in uniform normalized speeds: The outer boundary of the partially ionized zone has an initial radius $r_{\rm a0}$ and expand with $\beta_{\rm a}$. The boundary of the H II zone has an initial radius $r_{\rm b0}$ and expands with and $\beta_{\rm b}$ (with $\beta_{\rm b} \le \beta_{\rm a}$, which avoids the unphysical situation where the expansion of the H II zone overruns the expansion of the partially ionized zone). At $t = 0$, when the light front, propagating in the x-direction (as in the two-zone model) reaches the outer boundary of the partially ionized zone, which is located at $x = -r_{\rm a0}$. The results obtained above for the two-zone model can be adopted using the substitutions $r_0 \rightarrow r_{\rm a0}$ and $\beta \rightarrow \beta_{\rm a}$. The advancing of the light front is now $x(t) = -r_{\rm a0} + \xi(t)$, and the radius of the outer boundary of the partially ionized zone is $r(t) = r_{\rm a0} + \beta_{\rm a}\xi(t)$. Thus,

$$\left\{ \begin{array}{l} x = -r_{\rm a0} + \xi \, ; \\ y = \pm \Big\{ (1+\beta_{\rm a})\xi \left[2r_{\rm a0} - (1-\beta_{\rm a})\xi \right] \Big\}^{1/2} . \end{array} \right. \tag{11}$$

Also, we have

$$\xi_{\rm a(\pm)}\Big|_y = \frac{r_{\rm a0}}{(1-\beta_{\rm a})} \left\{ 1 \pm \left[1 - \left(\frac{1-\beta_{\rm a}}{1+\beta_{\rm a}} \right) \left(\frac{y}{r_{\rm a0}} \right)^2 \right]^{1/2} \right\} . \tag{12}$$

The corresponding maximum size of the partially ionized zone perceived by the distant observer is

$$y_{*\rm a} = \pm r_{\rm a0} \left(\frac{1+\beta_{\rm a}}{1-\beta_{\rm a}} \right)^{1/2} . \tag{13}$$

For the inner boundary of the partially ionized zone, some additional transformations for the corresponding variables are required, before applying the results obtained for the two-zone model. First, the light front reaches this boundary at a time $\tilde{t}$, at a location between $x = -r_{\rm a0}$ and $x = -r_{\rm b0}$. Denote this location as $x = -\tilde{r}_{\rm b0}$. We may then determine $\tilde{r}_{\rm b0}$, $\tilde{t}$, and hence $\tilde{\xi}(= c\tilde{t})$ by setting $-r_{\rm a0} + \tilde{\xi} = -r_{\rm b0} - \beta_{\rm b}\tilde{\xi}$. This gives

$$\tilde{\xi} = c\,\tilde{t} = \frac{r_{\rm a0} - r_{\rm b0}}{(1+\beta_{\rm b})} = r_{\rm a0} \left(\frac{1-\varpi}{1+\beta_{\rm b}} \right) , \tag{14}$$

and

$$\tilde{r}_{\rm b0} = \frac{\beta_b r_{\rm a0} + r_{\rm b0}}{(1+\beta_b)} = r_{\rm a0} \left(\frac{\varpi + \beta_{\rm b}}{1+\beta_{\rm b}} \right) , \tag{15}$$

where $\varpi = r_{\rm b0}/r_{\rm a0} \le 1$. With the substitutions of $r_{\rm a0} \rightarrow \tilde{r}_{\rm b0}$, $\beta_a \rightarrow \beta_b$, and $\xi \rightarrow (\xi - \tilde{\xi})$ in equations (11), (12), and (13), we obtain

$$\left\{ \begin{array}{l} x = -r_{\rm a0} + \xi = -\tilde{r}_{\rm b0} + (\xi - \tilde{\xi}) \, ; \\ y = \pm \Big\{ (1+\beta_{\rm b}) \left(\xi - \tilde{\xi} \right) \left[2\tilde{r}_{\rm b0} - (1-\beta_{\rm b}) \left(\xi - \tilde{\xi} \right) \right] \Big\}^{1/2} , \end{array} \right. \tag{16}$$

for the interception of the light front with the boundary of the H II zone. It follows that

$$\xi_{\rm b(\pm)}\Big|_y - \tilde{\xi} = \frac{\tilde{r}_{\rm b0}}{(1-\beta_{\rm b})} \left\{ 1 \pm \left[1 - \left(\frac{1-\beta_{\rm b}}{1+\beta_{\rm b}} \right) \left(\frac{y}{\tilde{r}_{\rm b0}} \right)^2 \right]^{1/2} \right\} , \tag{17}$$

implying that

$$\xi_{\rm b(\pm)}\Big|_y = r_{\rm a0} \left\{ \left(\frac{1-\varpi}{1+\beta_{\rm b}} \right) + \left(\frac{\varpi + \beta_{\rm b}}{1-\beta_{\rm b}^2} \right) \left[1 \pm f(y; \beta_{\rm b}, \varpi, r_{\rm a0}) \right] \right\} , \tag{18}$$

where

$$f(y; \beta_{\rm b}, \varpi, r_{\rm a0}) = \left[1 - \left(\frac{1-\beta_{\rm b}^2}{(\varpi + \beta_{\rm b})^2} \right) \left(\frac{y}{r_{\rm a0}} \right)^2 \right]^{1/2} \le 1 , \tag{19}$$

and is always positive. Also,

$$y_{*\rm b} = \pm \tilde{r}_{\rm b0} \left(\frac{1+\beta_{\rm b}}{1-\beta_{\rm b}} \right)^{1/2} = \pm r_{\rm a0} \left(\frac{(\varpi + \beta_{\rm b})^2}{1-\beta_{\rm b}^2} \right)^{1/2} . \tag{20}$$

In the context of radiative transfer (and ray-tracing), a fraction of the radiation (those at $|y_{*\rm a}| \ge |y| > |y_{*\rm b}|$) will pass through the partially ionized zone, and another fraction of the radiation (those at $|y_{*\rm b}| \ge |y|$) will pass through the partially ionized zone before entering the H II zone and then pass through the partially ionized zone later afterwards. For the rays at $|y_{*\rm a}| \ge |y| > |y_{*\rm b}|$, the specific optical depth, at frequency ν, across the H II and partially ionized zones is

$$\tau_\nu\Big|_y = \frac{2\kappa_{\nu \rm a} r_{\rm a0}}{(1-\beta_{\rm a})} \left[1 - \left(\frac{1-\beta_{\rm a}}{1+\beta_{\rm a}} \right) \left(\frac{y}{r_{\rm a0}} \right)^2 \right]^{1/2} , \tag{21}$$

where $\kappa_{\nu \rm a}$ is the specific opacity of the gas in the partially ionized zone. For rays with $|y_{*\rm b}| \ge |y|$, the specific optical depth is the sum of three components: two from the partially ionized zone and one form the H II zone. Along the ray, they are the segments of the light path specified by $(\zeta_{\rm a(-)}, \zeta_{\rm b(-)})$ for the first passage in the partially ionized zone, $(\zeta_{\rm b(-)}, \zeta_{\rm b(+)})$ for the passage in the H II zone, and $(\zeta_{\rm b(+)}, \zeta_{\rm a(+)})$ for the second passage in the partially ionized zone. We denote the corresponding specific optical depth for these three passages as $\tau_\nu^{\rm [i]}$, $\tau_\nu^{\rm [j]}$, and $\tau_\nu^{\rm [k]}$, respectively, and the total specific optical depth is the sum of them, i.e. $\tau_\nu = \tau_\nu^{\rm [i]} + \tau_\nu^{\rm [j]} + \tau_\nu^{\rm [k]}$.

Using similar procedures as in the derivation of equation (21), we obtain

$$\begin{aligned} \tau_\nu^{\rm [j]}\Big|_y &= 2\kappa_{\nu \rm b} r_{\rm a0} \left(\frac{\varpi + \beta_{\rm b}}{1-\beta_{\rm b}^2} \right) \left[1 - \left(\frac{1-\beta_{\rm b}^2}{(\varpi + \beta_{\rm b})^2} \right) \left(\frac{y}{r_{\rm a0}} \right)^2 \right]^{1/2} \\ &= 2\kappa_{\nu \rm b} r_{\rm a0} \left(\frac{\varpi + \beta_{\rm b}}{1-\beta_{\rm b}^2} \right) f(y; \beta_{\rm b}, \varpi, r_{\rm a0}) \end{aligned} \tag{22}$$

for the H II zone.[1] To derive the specific optical depths of the two passages through the partially ionized zone, we may consider the expression

$$\xi_{\rm a(\pm)}\Big|_y = \tfrac{r_{\rm a0}}{(1-\beta_{\rm a})} \left\{ 1 \pm f(y; \beta_{\rm a}, 1, r_{\rm a0}) \right\} \tag{23}$$

to simplify the algebraic steps. The specific optical depth corresponding to the first passage is

$$\begin{aligned} \tau_\nu^{\rm [i]}\Big|_y &= \kappa_{\nu \rm a} \left[\xi_{\rm b(-)} - \xi_{\rm a(-)} \right] \\ &= \kappa_{\nu \rm a} r_{\rm a0} \left\{ \left(\frac{1-\varpi}{1+\beta_{\rm b}} \right) + \left(\frac{\varpi + \beta_{\rm b}}{1-\beta_{\rm b}^2} \right) \left[1 - f(y; \beta_{\rm b}, \varpi, r_{\rm a0}) \right] \right. \\ &\quad \left. - \left(\frac{1}{1-\beta_{\rm a}} \right) \left[1 - f(y; \beta_{\rm a}, 1, r_{\rm a0}) \right] \right\} ; \end{aligned} \tag{24}$$

[1] We can recover equation (21) by setting $\varpi \rightarrow 1$, $\beta_{\rm b} \rightarrow \beta_{\rm a}$, and $\kappa_{\nu \rm b} \rightarrow \kappa_{\nu \rm a}$ in equation (22).

the specific optical depth corresponding to the second passage is

$$\begin{aligned}\tau_\nu^{[\mathrm{k}]}\big|_y &= \kappa_{\nu\mathrm{a}}\left[\xi_{\mathrm{a}(+)} - \xi_{\mathrm{b}(+)}\right] \\ &= \kappa_{\nu\mathrm{a}} r_{\mathrm{a}0}\left\{\left(\frac{1}{1-\beta_\mathrm{a}}\right)\left[1 + f(y;\beta_\mathrm{a},1,r_{\mathrm{a}0})\right] - \left(\frac{1-\varpi}{1+\beta_\mathrm{b}}\right)\right. \\ &\quad \left. - \left(\frac{\varpi+\beta_\mathrm{b}}{1-{\beta_\mathrm{b}}^2}\right)\left[1 + f(y;\beta_\mathrm{b},\varpi,r_{\mathrm{a}0})\right]\right\}. \end{aligned} \tag{25}$$

With non-zero $\kappa_{\nu\mathrm{a}}$ and $\kappa_{\nu\mathrm{b}}$, summing the specific optical depths in equations (22), (24), and (25) yields

$$\begin{aligned}\tau_\nu\big|_y &= 2\kappa_{\nu\mathrm{a}} r_{\mathrm{a}0}\left\{\left(\frac{1}{1-\beta_\mathrm{a}}\right) f(y;\beta_\mathrm{a},1,r_{\mathrm{a}0})\right. \\ &\quad \left. + \left(\frac{\kappa_{\nu\mathrm{b}}}{\kappa_{\nu\mathrm{a}}} - 1\right)\left(\frac{\varpi+\beta_\mathrm{b}}{1-{\beta_\mathrm{b}}^2}\right) f(y;\beta_\mathrm{b},\varpi,r_{\mathrm{a}0})\right\} \end{aligned} \tag{26}$$

for $|y_{*\mathrm{b}}| > |y|$. Note that the expression for the specific optical depth above becomes the same as that in equation (21), by equating $\kappa_{\nu\mathrm{b}}$ and $\kappa_{\nu\mathrm{a}}$, regardless of what values β_b takes. However, if we set $\varpi \to 1$ and $\beta_\mathrm{b} \to \beta_\mathrm{a}$ in equation (26), then equation (21) becomes a special case of it where $\kappa_{\nu\mathrm{b}}$ equals $\kappa_{\nu\mathrm{a}}$.

The structures of real ionized cavities are expected to be more complex than that of the two-zone and three-zone model bubbles. Ionized cavities produced by quasars and galaxies have been studied in detail with analytical (e.g. Shapiro & Giroux 1987; Wyithe & Loeb 2004), semi-numerical (e.g. Geil & Wyithe 2008; Mesinger et al. 2011), and hydrodynamical simulations (e.g. Thomas et al. 2009; Geil et al. 2017; Hutter et al. 2021; Kannan et al. 2022). While these studies focused on the global progression of reionization, some also targeted individual bubbles (e.g. Ghara et al. 2017). The statistics properties of the cavities were also investigated (e.g. Zahn et al. 2007; Shin, Trac & Cen 2008; Lin et al. 2016; Muñoz et al. 2022; Schaeffer, Giri & Schneider 2023; Lu et al. 2024). The 21-cm signals associated with complex ionization structures are not ideal for comparing our covariant formulation with the optical depth parametrization. Hence, we adopt the simplified two-zone and three-zone models.

2.3 Cosmological expansion

Cosmological expansion affects the observational properties different to the local expansions, such as the geometrical expansion caused by the advance of an ionization front. When the Universe expands, an ionized cavity expands accordingly, even when the ionization front is stationary in the local reference frame. Cosmological expansion also alters the thermodynamics and hydrodynamic properties of the ionized cavities. It sets a new balance between the radiative processes, hence modifying the radiation and the observational characteristics of the ionized cavity.

Two effects are the most noticeable among the others. (i) The size of the cavity perceived by an observer at a lower redshift is larger than the size of the cavity measured in its local reference frame, where the radiative and hydrodynamic processes operate. (ii) The wavelength of the radiation is stretched as it propagates across the cavity. A 21-cm line originated from the far side of the cavity will have a wavelength longer than 21 cm when it reaches another side of the cavity. This change in the wavelength will alter the transport of the radiation. For the 21-cm line, the interaction with its neighbouring continuum becomes prominent, while the resonance absorption can become insignificant. This has not taken account of further complications by effects associated with thermal and hydrodynamics evolution of the cavity and of the medium surrounding the cavity.

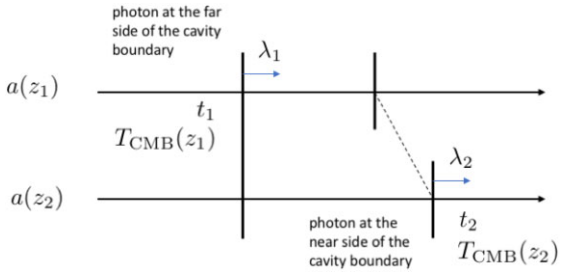

Figure 2. An illustration showing the changes in the properties of the radiation, e.g. its wavelength λ, and its environment, e.g. the CMB temperature T_{CMB}, along the LoS between the moment that it started propagating from the far side of the cavity boundary (with variables denoted by the subscript '1') and the moment that it reached the near side of the cavity boundary (with variables denoted by the subscript '2'), as perceived by a distant observer at present. A useful reference for the changes is the cosmological redshift z, which has a 1–1 correspondence to a cosmological time t. The rate of change in the scale factor a in the FLRW metric is a measure of the cosmological expansion, which may be parametrized by z or t. The same LoS is drawn twice in the figure to illustrate separately the conditions when the radiation started and finished its propagation across the cavity.

Fig. 2 shows an illustration to elaborate these effects. A photon of a wavelength λ_1 starts its journey from the far side of a cavity boundary, at redshift z_1 (corresponding to a cosmological time t_1) and arrives at the near side of the cavity boundary, at a lower redshift z_2 (corresponding to a cosmological time t_2). When the photon reached the other side of the cavity boundary its wavelength became λ_2. The cavity was bathed in the CMB of temperature $T_{\mathrm{CMB}}(z_1)$ at the moment the photon started its journey, but the temperature of the ambient CMB had dropped to a lower temperature $T_{\mathrm{CMB}}(z_2)$ by the time the photon arrived at the other side of the cavity.

In a Friedmann–Lemaître–Robertson–Walker (FLRW) universe with a zero curvature, the expansion of the universe can be parametrized by a scale parameter $a(t)$, which evolves with the cosmological redshift as

$$\frac{a(t_2)}{a(t_1)} = \frac{1+z_1}{1+z_2}\,. \tag{27}$$

This gives the stretch of the wavelength of radiation

$$\frac{\lambda_2}{\lambda_1} = \frac{a(t_2)}{a(t_1)} = \frac{1+z_1}{1+z_2}\,, \tag{28}$$

and the evolution of the CMB temperature

$$\frac{T_{\mathrm{CMB}}(z_2)}{T_{\mathrm{CMB}}(z_1)} = \frac{1+z_2}{1+z_1}\,. \tag{29}$$

The number density of particles evolves with the cosmological redshift as

$$\frac{n_2}{n_1} = \frac{n(z_2)}{n(z_1)} = \left(\frac{1+z_2}{1+z_1}\right)^3\,. \tag{30}$$

Consider that a photon propagates from a location r_1 to a location at r_2. It starts from r_1 at time t_1 and reaches r_2 at time t_2. As photons travel along null geodesics, in a flat FLRW universe $c\,\mathrm{d}\,t = a(t)\,\mathrm{d}\,r$ along the LoS. It follows that

$$\frac{1}{c}\int_{r_1}^{r_2} \mathrm{d}r = \int_{z_1}^{z_2} \mathrm{d}z\,(1+z)\left(\frac{\mathrm{d}t}{\mathrm{d}z}\right)\,. \tag{31}$$

Here z_1 and z_2 are the redshifts, with respect to a present observer located at $r = 0$ at redshift $z = 0$, respectively, and correspond to the time t_1 (when the photon starts its journey from r_1) and t_2 (the time

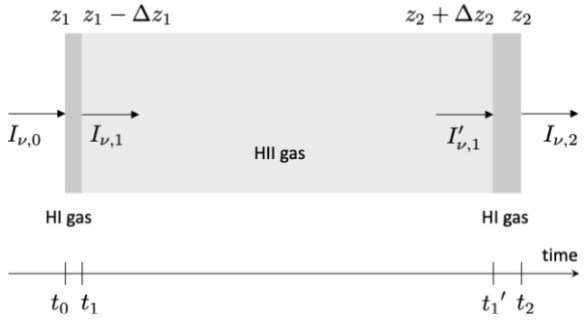

Figure 3. A schematic illustration of the three-slab model to show radiative transfer effects on line and continuum of radiation through an H II slab sandwiched by two initially identical thin H I slabs in an expanding universe. When the radiation enters the first H I slab, its specific intensity is $I_{\nu,0}$; when the radiation exits, it is $I_{\nu,1}$. When the radiation enters the second H I slab, its specific intensity is $I'_{\nu,1}$; when the radiation exits, it is $I_{\nu,2}$. The sequence of redshifts at which the radiation passes the slab boundaries in its propagation is $\{z_1, z_1 - \Delta z_1, z_2 + \Delta z_2, z_2\}$. The corresponding sequence of time is $\{t_0, t_1, t_1', t_2\}$.

when the photon completes its journey reaching r_2), with $a(t) = 1$ at $z = 0$. Hence, z_2 satisfies

$$\int_0^{z_2} \mathrm{d}z\,(1+z)\left(\frac{\mathrm{d}t}{\mathrm{d}z}\right) = \int_0^{z_1} \mathrm{d}z\,(1+z)\left(\frac{\mathrm{d}t}{\mathrm{d}z}\right) - \left(\frac{r_1 - r_2}{c}\right) . \tag{32}$$

In the Lambda cold dark matter framework,

$$\frac{\mathrm{d}t}{\mathrm{d}z} = -\left\{ H_0(1+z)\left[\Omega_{\mathrm{r},0}(1+z)^4 + \Omega_{\mathrm{m},0}(1+z)^3 + \Omega_{\Lambda,0}\right]^{1/2} \right\}^{-1} \tag{33}$$

(see e.g. Peacock 1999) where H_0 is the Hubble parameter at present, and $\Omega_{\mathrm{r},0}$, $\Omega_{\mathrm{m},0}$, and $\Omega_{\Lambda,0}$ are the density parameters for radiation, matter, and dark energy, respectively. For the spherical H II zones in the two-zone model without expansion induced by ionization (Fig. 1, see also Section 2.2), $(r_1 - r_2) = -2r_0$ along the symmetry axis. With this specified, z_2 is readily determined for a given z_1, and this can be generalized for the two-zone and three-zone models. Assigning the location of the zone boundaries as r_2, which specifies the value for $(r_1 - r_2)$. The corresponding z_2 (and hence t_2) can be obtained by a direction integration of equation (32). During the dark ages and the EoR, the cosmological evolution is matter dominated. We may ignore $\Omega_{\mathrm{r},0}$ and $\Omega_{\Lambda,0}$, which results in an analytic expression for z_2:

$$z_2 = \left(\frac{1}{\sqrt{1+z_1}} - \left(\frac{r_1 - r_2}{c}\right)\frac{H_0\sqrt{\Omega_{\mathrm{m},0}}}{2} \right)^{-2} - 1 . \tag{34}$$

We now use a three-slab model to illustrate the difference between the spectra, consisting of a line component and a continuum component, in the presence and in the absence of cosmological expansion.

Consider a ray of radiation with initial specific intensity $I_{\nu,0}$, passing through a slab of H II gas sandwiched by two thermal absorptive slabs of H I gas, both of comoving thickness δs (see Fig. 3). Without losing generality, the total optical depth of the H II slab is assumed to be negligible, i.e. the slab practically does not contribute to absorption and emission of the radiation. The two H I slabs are transparent to the continuum but have sufficient optical depths at the line centre frequency, $\nu_{21\mathrm{cm}}$, and its neighbouring frequencies. The local absorption in the H I slabs is specified by an absorption coefficient, which takes the form: $\kappa_\nu = n_{\mathrm{a}}\,\sigma_{\mathrm{a}}\,\phi(\nu - \nu_{21\mathrm{cm}})$, where n_{a} is the number density of the absorbers, σ_{a} is the normalized absorption cross-section, $\nu_{21\mathrm{cm}}$ is the centre frequency measured in the local rest frame, and $\phi(\nu - \nu_{21\mathrm{cm}})$ is a normalized line profile function, i.e.

$$\int_0^\infty \mathrm{d}\nu\ \phi(\nu - \nu_{21\mathrm{cm}}) = 1 . \tag{35}$$

A thermal absorptive media also emits and the local emissivity can be derived from the absorption coefficient and the source function, which is the Planck function $B_\nu(T)$ in a thermal medium. (Note that, for simplicity, we have omitted the contribution from stimulated emission in this illustration. For the radiative transfer calculations of the hyperfine 21-cm H I line used for diagnosing cosmological reionization, stimulated emission must be included.)

At low frequencies (i.e. in the Rayleigh–Jeans regime), the Planck function $B_\nu \rightarrow I^{\mathrm{RJ}}{}_\nu = b\nu^2 T$, where $b = 2k_{\mathrm{B}}c^{-2}$ and k_{B} is the Boltzmann constant. For $\Delta z_1 \ll (1+z_1)$ and $\Delta z_2 \ll (1+z_2)$, we may approximate that the emission and absorption are constant with time. Suppose also that the background is a thermal blackbody of a temperature T_0. Then, in this situation,

$$\begin{aligned} I_{\nu,1} &= I_{\nu,0}\exp(-n_{\mathrm{a},1}\sigma_{\mathrm{a}}\phi(\nu - \nu_{21\mathrm{cm}})\delta s) \\ &\quad + B_\nu(T_1)\left[1 - \exp(-n_{\mathrm{a},1}\sigma_{\mathrm{a}}\phi(\nu - \nu_{21\mathrm{cm}})\delta s)\right] \\ &= b\nu^2\Big[T_0\exp(-n_{\mathrm{a},1}\sigma_{\mathrm{a}}\phi(\nu - \nu_{21\mathrm{cm}})\delta s) \\ &\quad + T_1\left[1 - \exp(-n_{\mathrm{a},1}\sigma_{\mathrm{a}}\phi(\nu - \nu_{21\mathrm{cm}})\delta s)\right]\Big] , \end{aligned} \tag{36}$$

where $n_{\mathrm{a},1}$ is the number density of absorber in H I slab 1 and T_1 is the thermal temperature associated with the line-formation process in H I slab 1. As the H II slab does not contribute to absorption and emission, (I_ν/ν^3) is invariant. Thus,

$$\begin{aligned} I'_{\nu,1} &= b\nu^2\left(\frac{1+z_2}{1+z_1}\right)^3\Big[T_0\exp(-n_{\mathrm{a}}(z_1)\sigma_{\mathrm{a}}\phi(\nu - \nu^*_{21\mathrm{cm}})\delta s) \\ &\quad + T_1\left[1 - \exp(-n_{\mathrm{a}}(z_1)\sigma_{\mathrm{a}}\phi(\nu - \nu^*_{21\mathrm{cm}})\delta s)\right]\Big] , \end{aligned} \tag{37}$$

where $\nu^*_{21\mathrm{cm}} = \nu_{21\mathrm{cm}}(1+z_2)/(1+z_1)$, and

$$\begin{aligned} I_{\nu,2} &= b\nu^2\Big\{\left(\frac{1+z_2}{1+z_1}\right)^3\exp(-n_{\mathrm{a},2}\sigma_{\mathrm{a}}\phi(\nu - \nu_{21\mathrm{cm}})\delta s) \\ &\quad \times\Big[T_0\exp(-n_{\mathrm{a},1}\sigma_{\mathrm{a}}\phi(\nu - \nu^*_{21\mathrm{cm}})\delta s) \\ &\quad + T_1\left[1 - \exp(-n_{\mathrm{a},1}\sigma_{\mathrm{a}}\phi(\nu - \nu^*_{21\mathrm{cm}})\delta s)\right]\Big] \\ &\quad + T_2\left[1 - \exp(-n_{\mathrm{a},2}\sigma_{\mathrm{a}}\phi(\nu - \nu_{21\mathrm{cm}})\delta s)\right]\Big\} , \end{aligned} \tag{38}$$

where $n_{\mathrm{a},2}$ is the number density of absorber in H I slab 2 and T_2 is the thermal temperature associated with the line-formation process in H I slab 2. Generally, $T_0 \neq T_1 \neq T_2$ and $n_{\mathrm{a},1} \neq n_{\mathrm{a},2}$. The spectrum of the radiation that emerges has a continuum component and two line components, one associated the absorption in H I slab 1 and another associated with the absorption in H I slab 2. The continuum has a specific intensity

$$I_{\nu,2} = b\nu^2\left(\frac{1+z_2}{1+z_1}\right)^3 T_0 , \tag{39}$$

which is independent of the thermal conditions in the two H I slabs. This is consistent with our assumption that the two H I slabs are optically thin to the continuum and the H II slab has no contribution to the radiation, and that $\nu^{-3}I_\nu$ is an invariant quantity. For a sufficiently large difference between z_1 and z_2 such that the two line-profile functions do not overlap, the line associated with the first H I slab is centred at $\nu^*_{21\mathrm{cm}} = \nu_{21\mathrm{cm}}(1+z_2)/(1+z_1)$, and the specific intensity

at the line centre is

$$I_{\nu,1} = b\nu^2 \left(\frac{1+z_2}{1+z_1}\right)^3 \left[(T_0 - T_1)\exp(-n_{\rm a,1}\sigma_{\rm a}\phi(0)\delta s) + T_1\right]. \tag{40}$$

The line associated with the second H I slab is centred at $\nu_{21\rm cm}$, and the specific intensity at the line centre is

$$I_{\nu,2} = b\nu^2 \left\{\left[\left(\frac{1+z_2}{1+z_1}\right)^3 T_0 - T_2\right]\exp(-n_{\rm a,2}\sigma_{\rm a}\phi(0)\delta s) + T_2\right\}. \tag{41}$$

Here, it shows the two line components are not identical with the correction of the shift in the line centre energies, even for identical thermal conditions in the two H I slabs at time t_0, when the radiation enters the first H I slab. Even when the micro-astrophysical processes, such as heating and photon-pumping are absent, cosmological expansion would alter the temperature and the number density of the absorbers in the slabs. If cosmological expansion is insignificant over the interval when the radiation completes its journey through the two H I slabs and the H II slab, the spectrum has a continuum and only one line. The specific intensity of the continuum is simply

$$I_{\nu,2} = b\nu^2 T_0\,. \tag{42}$$

The line is centred at frequency $\nu_{21\rm cm}$, and the specific intensity at the line centre is

$$I_{\nu,2} = b\nu^2\Big[(T_0 - T_1)\exp(-(n_{\rm a,1} + n_{\rm a,2})\sigma_{\rm a}\phi(0)\delta s) + (T_1 - T_2)\exp(-n_{\rm a,2}\sigma_{\rm a}\phi(0)\delta s) + T_2\Big]\,. \tag{43}$$

The line-centre specific intensity becomes the same as the specific intensity of the continuum neighbouring to the line, i.e. the line vanishes, when $T_2 = T_1 = T_0$. An emission line will result for $T_0 > T_1 > T_2$ and an absorption line will result for $T_2 > T_1 > T_0$. These results are as expected from the line-formation criteria.

The effect of cosmological expansion in the transport of ionizing photons and the development of ionized cavities have been studied analytically and implemented in reionization simulations (see e.g. Shapiro & Giroux 1987; Weber et al. 2013; Bisbas et al. 2015; Fedchenko & Krasnobaev 2018). The subsequent effects on 21-cm signals are also discussed (Yu 2005). This cosmological effect is sometimes named as 'light-cone effect' and may lead to anisotropy in the 21-cm power spectrum (Barkana & Loeb 2006; Datta et al. 2012; La Plante et al. 2014). However, this effect is generally ignored in recent studies of 21-cm signals which are based on reionization simulations.

3. COMPUTATIONAL SET-UP FOR 21-CM RADIATIVE TRANSFER CALCULATION

We briefly recapitulate the C21LRT equation and the input default reionization history model used throughout this paper first. The computational set-up for the radiative transfer calculations is the same as in Chan et al. (2023), except for the inserted H II zones.

The C21LRT equation in covariant form with our adopted FLRW cosmological model, when there is negligible scattering, is as follows:

$$\frac{\rm d}{{\rm d}z}\left(\frac{I_{\rm L,\nu}}{\nu^3}\right) = (1+z)\left[-\left(\kappa_{\rm C,\nu} + \kappa_{\rm L,\nu}\,\phi_\nu\,[1-\Xi]\right)\left(\frac{I_{\rm L,\nu}}{\nu^3}\right) + \frac{(\epsilon_{\rm C,\nu} + \epsilon_{\rm L,\nu}\,\phi_\nu)}{\nu^3}\right]\frac{{\rm d}s}{{\rm d}z}\,, \tag{44}$$

where the subscript 'L' and 'C' denote the 21-cm line and its neighbouring continuum (i.e. CMB in our calculations). Following their definitions in the previous section, $I_{\rm L,\nu}$, $\kappa_{\rm L,\nu}$, and $\epsilon_{\rm L,\nu}$ are the specific intensity, line absorption coefficient, and line emission coefficient at 21-cm line centre, respectively. Ξ is the factor for the stimulated emission. $\kappa_{\rm C,\nu}$ and $\epsilon_{\rm C,\nu}$ are the continuum absorption coefficient and continuum emission coefficient and ϕ_ν is the normalized line-profile functions. s represents the photon's path-length, and ${\rm d}s/{\rm d}z = c\,{\rm d}t/{\rm d}z$ can be calculated based on our assumed cosmology (see equation 33).

The line coefficients are calculated in a local rest frame (the same practice as in Fuerst & Wu 2004; Younsi, Wu & Fuerst 2012; Chan et al. 2019) as follows:

$$\epsilon_{\rm L,\nu} = \frac{h\nu_{\rm ul}}{4\pi}\,n_{\rm u}A_{\rm ul}, \tag{45}$$

$$\kappa_{\rm L,\nu} = \frac{h\nu_{\rm ul}}{4\pi}\,n_{\rm l}B_{\rm lu} = \frac{1}{8\pi}\left(\frac{c}{\nu_{\rm ul}}\right)^2\left(\frac{g_{\rm u}}{g_{\rm l}}\right)n_{\rm l}A_{\rm ul}, \tag{46}$$

where the subscript 'u' denotes the upper energy state and 'l' denotes the lower energy state of the H I hyperfine transition. Here, $\nu_{\rm ul} = \nu_{21\rm cm}$, $g_{\rm u}$ and $g_{\rm l}$ are the multiplicities (degeneracies) of the upper and lower energy states, respectively, $n_{\rm u}$ and $n_{\rm l}$ are the number density of particles in the upper and lower energy states, respectively, and $A_{\rm ul}$ and $B_{\rm ul}$ are the Einstein coefficients. We assume that the normalized line profile functions $\phi_{\nu,\rm x} \equiv \phi_{\rm x}(\nu - \nu_{\rm line,0})$, with ${\rm x} \in \{\rm abs, emi, sti\}$ corresponding to absorption, spontaneous emission, and stimulated emission, respectively. Then the factor for the stimulated emission is $\Xi = (n_{\rm u}g_{\rm l})/(n_{\rm l}g_{\rm u})$.

With this C21LRT equation, the input H I gas properties in EoR are the globally averaged spin temperature $T_{\rm s}(z)$ and ionized fraction $x_{\rm i}(z)$ from the 'EOS 2021 all galaxies simulation result' (which used the 21CMFAST code) (Muñoz et al. 2022). The density of H I gas is calculated based on $x_{\rm i}$ and the adopted cosmological model. Then $n_{\rm u}$ and $n_{\rm l}$ are calculated with $T_{\rm s}$. We only consider CMB and leave other types of continuum emission to future studies. One 21-cm line profile is adopted for all redshifts throughout one calculation and it is parametrized as follows:

$$\phi(\nu - \nu_{21\rm cm}) = \frac{1}{\sqrt{\pi}\Delta\nu_{\rm D}}\exp\left[-\left(\frac{\nu - \nu_{21\rm cm}}{\Delta\nu_{\rm D}}\right)^2\right] \tag{47}$$

where

$$\Delta\nu_{\rm D} = \nu_{21\rm cm}\sqrt{\frac{2k_{\rm B}T_{\rm k}}{mc^2} + \left(\frac{v_{\rm turb}}{c}\right)^2} \tag{48}$$

is the Doppler parameter.

As little do we know about the turbulent velocity of H I gas, from observations or from reliable theoretical modelling, in the ionization front created by luminous sources, we choose the turbulent velocity of gas in intra-cluster medium (ICM), intergalactic medium (IGM), and inter stellar medium (ISM) as benchmarks. The characteristic $v_{\rm turb}$ for ICM is $\sim 100\,{\rm km\,s^{-1}}$, created by large-scale shocks (Schuecker et al. 2004; Subramanian, Shukurov & Haugen 2006; Parrish, Quataert & Sharma 2010; Ruszkowski & Oh 2011; Vazza et al. 2017; Hitomi Collaboration et al. 2018; Basu & Sur 2021). For IGM, turbulence can be caused by structure formation, galaxy merger, and galactic outflows (Xu & Zhang 2020) with $v_{\rm turb} \sim 1{-}10\,{\rm km\,s^{-1}}$ reported in simulation studies (Evoli & Ferrara 2011; Schmidt 2015; Zhang & Wang 2022) and also for observations of Lyman α forest (Bolton et al. 2022). For ISM, $v_{\rm turb} \sim 1{-}10\,{\rm km\,s^{-1}}$ (Oliva-Altamirano et al. 2018; Patrício et al. 2018) and can the turbulence can be driven by cold gas infall, gravitational instability, or star-formation activities (Patrício et al. 2018). We therefore adopt $v_{\rm turb} \sim 1,\ 10,\ 100\,{\rm km\,s^{-1}}$ in our calculations. As will be demonstrated, the exact value of $v_{\rm turb}$

does not affect our conclusions. We then assume that T_k is always 0 in this paper.[2]

More detailed description of the C21LRT formulation and the adopted default reionization history can be found in Chan et al. (2023).

With the default reionization history specified, we then insert H II zones of spherical shapes (referred as 'bubbles' in the following texts). Various methods have been employed in the literature to extract the topology and size distributions of ionized cavities from large-scale simulation studies (e.g. Furlanetto et al. 2006a; Shin et al. 2008; Friedrich et al. 2011; Lin et al. 2016). These studies predict the distribution of sizes of ionized cavities and study the evolution of the distribution function throughout EoR. The characteristic sizes vary from $\lesssim$1 Mpc at the beginning of EoR to $\gtrsim$10 Mpc at the end of EoR (Iliev et al. 2006; Shin et al. 2008; Friedrich et al. 2011; Lin et al. 2016). To cover the possible sizes, we choose bubble diameters d of 0.01, 0.1, 1.0, 10.0 Mpc. Only one bubble is inserted in each scenario. For most of the scenarios, radiative transfer calculation is carried out along a single ray through the bubble centre. The comoving distance intercepted by the ray is d. We always fix the boundary of the bubble at higher redshift, e.g. $z_{\rm begin} = 12.0$ first. With the size dz of the bubble specified by d, we then calculate the boundary of the bubble at lower redshift $z_{\rm end} = z_{\rm begin} - {\rm d}z$. Along this ray, $n_{\rm H\,I} = 0$ in the redshift cells between $z_{\rm begin}$ and $z_{\rm end}$. We insert bubbles in this way to facilitate the comparison of bubble features. We do not modify T_s in these redshift cells (as this should cause no difference). Each bubble in our calculation is resolved with at least 10 redshift cells.

Unless otherwise stated, the maximum likelihood cosmological parameters obtained by the Planck Collaboration XIII (2016a) are used in this work. At the present time, the Hubble parameter is $H_0 = 100\,h_0 = 67.74\ {\rm km\,s^{-1}\,Mpc^{-1}}$, the matter density is $\Omega_{\rm m,0} = 0.3089$, the cosmological constant or vacuum density is $\Omega_{\Lambda,0} = 0.6911$, and the radiation density is $\Omega_{\rm r,0} = 4.1650 \times 10^{-5}(h_0)^{-2}$ (Wright 2006).

4. RESULTS AND DISCUSSIONS

4.1 Results

4.1.1 What determines the properties of bubble features

We can first estimate the frequency range where the 21-cm spectra are affected by a bubble specified with $z_{\rm begin}$ and $z_{\rm end}$. Its effective size when measured in frequency (at $z = 0$) d$\nu_{\rm bubble}$ is

$$ {\rm d}\nu_{\rm bubble} = \nu_{\rm 21cm}[(1+z_{\rm end})^{-1} - (1+z_{\rm begin})^{-1}]. \quad (49) $$

It is natural to assume that the spectrum will be affected in frequencies from $\nu_{\rm 21cm}(1+z_{\rm end})^{-1}$ to $\nu_{\rm 21cm}(1+z_{\rm begin})^{-1}$. We also expect the 'neighbouring' frequencies to be affected due to the finite width of 21-cm line. The full width at half-maximum (FWHM) of the 21-cm line profile when measured with frequency in the local rest frame is

$$ \begin{aligned} {\rm FWHM}_\nu &= 2\sqrt{\ln 2}\left(\frac{v_{\rm turb}}{c}\right)\nu_{\rm 21cm} \\ &\approx 0.7889\left(\frac{v_{\rm turb}}{100\ {\rm km\,s^{-1}}}\right)\ {\rm MHz}. \end{aligned} \quad (50) $$

[2]To match $v_{\rm turb} = 10\,{\rm km\,s^{-1}}$, $T_k = 6060.67$ K which is already higher than the expected globally averaged temperature of H I (cf. fig. 1 of Chan et al. 2023). Also, such a high temperature is usually accompanied with high ionization fraction x_i, diminishing the 21-cm signal from H I gas.

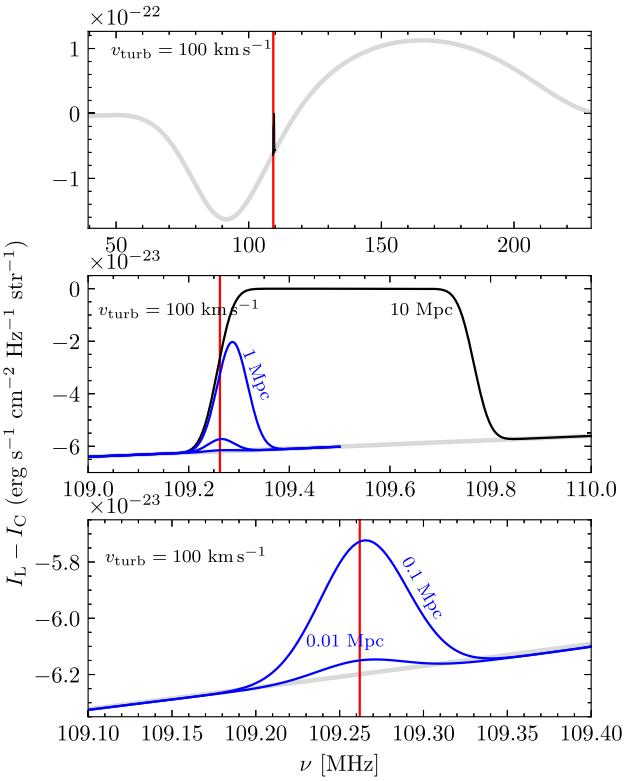

Figure 4. Features in the 21-cm spectra at $z = 0$ created by bubbles at $z_{\rm begin} = 12$. All the spectra in this figure are calculated with $v_{\rm turb} = 100\ {\rm km\,s^{-1}}$. The boundary of all the bubbles at the high-redshift end $z_{\rm begin} = 12.0$, which corresponds to $\nu = 109.2620$ MHz, is marked with red vertical line in all three panels. In the top panel, the globally averaged 21-cm spectrum without any bubble is plotted in thick grey line. The bubble features created by bubbles with diameters $d = 0.01, 0.1, 1.0, 10.0$ Mpc are also plotted with think black lines in contrast. The bubble features are not distinguishable from each other in this panel and are shown in more details in the middle and bottom panels. $z = 12.0$ is inside the absorption regime and all the bubble features can be understood as the decrease of the absorption signal. In the middle panel, the features created by bubbles with $d = 10.0, 1.0, 0.1$ Mpc are plotted in black with solid, dashed, and dash–dotted lines. The original 21-cm spectra (in grey) and the features created by smaller bubbles (in blue) are also preserved in this panel for comparison. The transition between a bump and a valley happened when the bubble is $\gtrsim$10 Mpc, this transition bubble size is mostly determined by $v_{\rm turb}$ as explained in the main text. In the bottom panel, the features created by bubbles with $d = 0.01, 0.1$ Mpc are plotted in blue. The original spectra is plotted in grey but not visible as the curve representing $d =$ 0.01 Mpc is almost identical in this panel.

Due to cosmological expansion, a 21-cm line with FWHM$_\nu$ at z will become narrower, i.e. $\nu_\phi = {\rm FWHM}_\nu \frac{1}{1+z}$ when propagated to $z = 0$. We therefore expect the spectrum to be affected at frequencies $\nu_{\rm 21cm}(1+z_{\rm end})^{-1} \pm {\rm d}\nu_\phi$ and $\nu_{\rm 21cm}(1+z_{\rm begin})^{-1} \pm {\rm d}\nu_\phi$. Note that we defined both d$\nu_{\rm bubble}$ and dν_ϕ at $z = 0$ to facilitate the analysis of bubble features in the observed spectra, which are at $z = 0$.

This estimation is consistent with the C21LRT results. We first analysed scenarios at $z = 12.0$ calculated with $v_{\rm turb} = 100\ {\rm km\,s^{-1}}$ as shown in Fig. 4. The original spectra without any bubble is plotted with thick grey line and the spectra with various bubble sizes in black in the top panel. In the middle panel, we zoomed into the relevant frequency range for the inserted bubbles. The smaller bubbles with $d = 0.01, 0.1, 1$ Mpc are plotted in blue. Their effective widths are d$\nu_{\rm bubble} = 4.9572 \times 10^{-4}, 4.9574 \times 10^{-3}, 4.9670 \times 10^{-2}$ MHz,

respectively, at $z = 0$. These bubbles are narrower than the width of 21-cm line profile ($\mathrm{d}\nu_{\rm bubble} \ll \mathrm{d}\nu_\phi = 0.06069$ MHz), and the spectral width of the bubble feature (at $z = 0$) $\mathrm{d}\nu_{\rm feature}$ is dominated by $\mathrm{d}\nu_\phi$. The effective size of the 10 Mpc bubble (5.0018×10^{-1} MHz) is larger than $\mathrm{d}\nu_\phi$. The corresponding bubble feature is plotted in black, with width dominated by $\mathrm{d}\nu_{\rm bubble}$. It is significantly broadened to be plateaus instead of bumps. The absolute value of specific intensity ($|I_{\rm L} - I_{\rm C}|$) is reduced to 0 at the plateau. In the bottom panel, we zoom in further to show the shape of the features created by smaller bubbles. Comparing the three curves calculated with $d = 0.01, 0.1$ Mpc, we can see that whilst the widths of the bubble features are similar (dominated by $\mathrm{d}\nu_\phi$), the heights of these features increase as the sizes of the bubble increase.

The analysis of bubbles in the emission regime of the redshifted 21-cm global signal is similar. These bubbles have $d = 0.01$–10 Mpc at $z_{\rm begin} = 8.0$. Their features are also calculated with $v_{\rm turb} = 100\ \mathrm{km\,s^{-1}}$ as shown in Fig. 5. Bubbles manifest as dips or valleys (reduced emission) as shown in the top panel. We zoomed into the bubble region in the middle panel. The bubble features created by small bubbles ($d = 0.01, 0.1, 1$ Mpc, $\mathrm{d}\nu_{\rm bubble} = 5.9570 \times 10^{-4}, 5.9572 \times 10^{-3}, 5.9697 \times 10^{-2}$ MHz) have a dip like shape (in blue). The 10 Mpc bubble (5.9989×10^{-1} MHz) has effective size larger than $\mathrm{d}\nu_\phi = 0.8766$ MHz and produce a valley-like shape. The transition between these two types of shapes is also determined by $\mathrm{d}\nu_\phi$. The features of smaller bubbles are enlarged in the bottom panel. Their depths also increase with the size of the bubble $\mathrm{d}\nu_{\rm bubble}$.

In the aforementioned results, we chose a large turbulent velocity ($v_{\rm turb} = 100\ \mathrm{km\,s^{-1}}$) to clearly demonstrate features created by the bubbles of $d = 0.01$–10 Mpc, also the transitions from dip (peak) to valley (plateau) when bubble sizes increases in emission (absorption) regime. As the transition is determined by comparing $\mathrm{d}\nu_{\rm bubble}$ to $\mathrm{d}\nu_\phi$, the critical bubble size where the transition happens is determined by $\mathrm{d}\nu_\phi$ (which is determined by $v_{\rm turb}$ in our calculation). To demonstrate this dependence, we also calculated the bubble features at $z = 12$ with $v_{\rm turb} = 10\ \mathrm{km\,s^{-1}}$, as shown in Fig. 6. The line profile width for this $v_{\rm turb}$ is $\mathrm{d}\nu_\phi = 0.006069$ MHz. In the top panel, the transition now happens between $d = 0.1$ Mpc and $d = 1$ Mpc (the transition happens between $d = 1$ Mpc and $d = 10$ Mpc for $v_{\rm turb} = 100\ \mathrm{km\,s^{-1}}$ in the middle panel of Fig. 4).

4.1.2 *Analytical approximations for bubble features*

For a $d = 0.01$ Mpc bubble at $z = 12.0$, its effective size $\mathrm{d}\nu_{\rm bubble} = 4.9572 \times 10^{-4}$ MHz is smaller than the line profile width $\mathrm{d}\nu_\phi$ when adopting turbulent velocities $v_{\rm turb} = 100,\ 10\ \mathrm{km\,s^{-1}}$. The width of the bubble features calculated with these $v_{\rm turb}$ are therefore all dominated by $\mathrm{d}\nu_\phi$. We then fit the features created with $d = 0.01$ Mpc with the line profile function (i.e. Gaussian functions in our calculations) for a more quantitative analysis.

The fitting results in Fig. 7 are for $v_{\rm turb} = 100$ and $10\ \mathrm{km\,s^{-1}}$ in the upper and lower panel. The bubble features calculated with C21LRT (black solid lines) and the fitted Gaussian functions (yellow dashed lines) are consistent over the frequency ranges from $(\nu_{21\rm cm} - 1.5\mathrm{FWHM}_\nu)/(1+z)$ to $(\nu_{21\rm cm} + 1.5\mathrm{FWHM}_\nu)/(1+z)$, where the fitting was carried out. The frequency corresponding to the high-redshift boundary $z_{\rm begin} = 12.0$ of all these bubbles are marked with red vertical lines. The fitted width $\mathrm{d}\nu_{\rm fit}$ and height $A_{\rm fit}$ of the Gaussian functions are listed in Table 1. The fitted width $\mathrm{d}\nu_{\rm fit}$ for the two bubble features are very close to $\mathrm{d}\nu_\phi$ as determined by $v_{\rm turb}$. Also, $A_{\rm fit}$ is very close to the maximum specific intensity of the bubble feature $I_{\rm max}$.

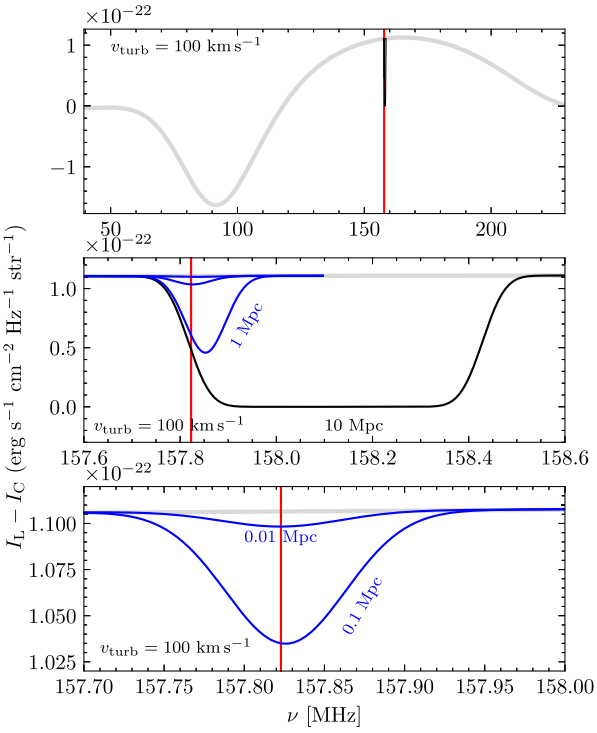

Figure 5. Features in the 21-cm spectra at $z = 0$ created by bubbles at $z_{\rm begin} = 8.0$. All the spectra in this figure are calculated with $v_{\rm turb} = 100\ \mathrm{km\,s^{-1}}$. The boundary of all the bubbles at the high-redshift end $z_{\rm begin} = 8.0$, which corresponds to $\nu = 157.8229$ MHz, is marked with red vertical line in all three panels. $z_{\rm begin} = 8.0$ is inside the emission regime and all the bubble features can be understood as decreasing of the emission signal. In the top panel, the globally averaged 21-cm spectrum without any bubble is plotted in thick grey line. The bubble features created by bubbles with diameters $d = 0.01, 0.1, 1.0, 10.0$ Mpc are also plotted with thin black lines in contrast. The bubbles features by larger bubbles and smaller bubbles are shown in more details in the middle and bottom panels. In the middle panel, the features created by bubbles with $d = 10.0, 1.0, 0.1$ Mpc are plotted in black with solid, dashed, and dash–dotted lines. The original 21-cm spectra (in grey) and the features created by smaller bubbles (in blue) are also preserved in this panel for comparison. The transition between a dip and a valley happened when the bubble is $\gtrsim$10 Mpc, this transition bubble size is mostly determined by $v_{\rm turb}$ as explained in the main text. In the bottom panel, the features created by bubbles with $d = 0.01, 0.1$ Mpc are plotted in blue. The original spectra is plotted in grey but not visible as the curve representing $d = 0.01$ Mpc is almost identical in this panel.

We calculated the relative difference between the bubble feature and the fitted Gaussian function and averaged it over from $(\nu_{21\rm cm} - 1.5\mathrm{FWHM}_\nu)/(1+z)$ to $(\nu_{21\rm cm} + 1.5\mathrm{FWHM}_\nu)/(1+z)$.[3] The averaged relative difference $\bar{\delta}$ for the two bubble features is all less than 10^{-4}. The small values of $\mathrm{d}\nu_\phi - \mathrm{d}\nu_{\rm fit}$, $I_{\rm max} - A_{\rm fit}$, and $\bar{\delta}$ show that the bubble features are very close to Gaussian functions and the bubble width is well approximated with $\mathrm{d}\nu_\phi$.

We then analyse the height of the feature $A_{\rm fit}$ of these bubble features. As discussed above, $A_{\rm fit}$ grows with $\mathrm{d}\nu_{\rm bubble}$. We also expect it to be proportional to the 21-cm emission coefficient.[4] We found

[3]The frequency cells are equally spaced in log space and no weighting was added when calculating the average.

[4]The 21-cm absorption coefficient in C21LRT is determined by the correction due to stimulated emission, which is much smaller than the emission coefficient.

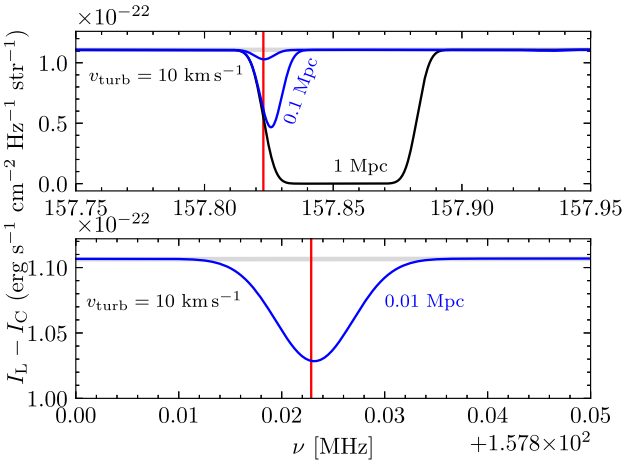

Figure 6. Features in the 21-cm spectra at $z = 0$ created by bubbles at $z_{\rm begin} = 12$. All the spectra in this figure are calculated with $v_{\rm turb} = 10$ km s^{-1}. In the top panel, the globally averaged 21-cm spectrum without any bubble is plotted in thick grey line (identical with some of the blues curved hence not visible). The bubble features created by bubbles with diameters $d = 0.01, 0.1, 1.0$ Mpc are plotted in this panel. Due to a smaller $v_{\rm turb}$, the transition between a bump and a valley happened when the bubble is $\gtrsim$1 Mpc. In the bottom panel, the features created by bubbles with $d = 0.01, 0.1$ Mpc are plotted in blue. The original spectra is plotted in grey, although only visible in the bottom panel. The frequency $\nu = 109.2620$ MHz corresponding to $z_{\rm begin} = 12.0$ is marked with red vertical lines in both panels.

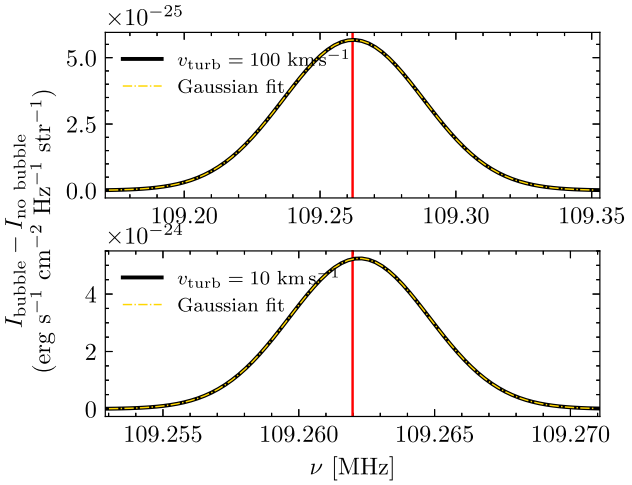

Figure 7. Gaussian fit analysis of the features created by a $d = 0.01$ Mpc bubble at $z = 12.0$. In all three panels, the difference between the original spectra ($I_{\rm nobubble}$) and the spectra when there is a $d = 0.01$ Mpc bubble at $z = 12.0$ ($I_{\rm bubble}$) is plotted with black solid lines. The difference in spectra ($I_{\rm bubble} - I_{\rm nobubble}$–$\nu$) is then fitted with a Gaussian function, shown in yellow dashed curves. From top to bottom panel, the bubble features were calculated with $v_{\rm turb} = 100,\ 10$ km s^{-1}, respectively. As explained in the main text, the widths of Gaussian features are dominated by the line profiles because a 0.01 Mpc bubble at $z = 12.0$ is narrower compared with the widths of the line profiles, when measured in frequency. The amplitudes of the Gaussian features can be approximated as $I_{\rm bubble} - I_{\rm nobubble} \sim d \cdot \epsilon_{{\rm L},\nu_{21\,\rm cm}}$, see main text for details.

that $A_{\rm fit}$ can be approximated as

$$A_{\rm fit} \approx C_{\rm convolution} \cdot I_{\rm analytical} = C_{\rm convolution} \cdot C_{{\rm d}\nu} \cdot C_{\rm redshift} \cdot d \cdot \epsilon_{{\rm L},\nu_{21\rm cm}}, \quad (51)$$

where $C_{\rm redshift} = (1+z)^3$ results from cosmological expansion (we may view this the factor as the ν^{-3} factor in the expression of the invariant intensity). $C_{{\rm d}\nu} = 1 + z$ is caused by the width of the relevant integration frequency range scales as $1 + z$ when the features propagate from z to the observer on Earth. The $C_{\rm convolution}$ factor resulted from convolution effect of line broadening in the local rest frames and the propagation of radiation. The values of $I_{\rm analytical}$ for the three bubble features are also listed in Table 1. By comparing $A_{\rm fit}$ with $I_{\rm analytical}$, the value of $C_{\rm convolution}$ is approximately 0.75.

These three examples are calculated with fixed ${\rm d}\nu_{\rm bubble}$ and different ${\rm d}\nu_\phi$. The results show that when the bubble feature is dominated by the line profile (${\rm d}\nu_{\rm bubble} \ll {\rm d}\nu_\phi$), the width of its spectral signature is well approximated by ${\rm d}\nu_\phi$. The height of the bubble's spectral feature is proportional to ${\rm d}\nu_{\rm bubble}/{\rm d}\nu_\phi$ and can be approximated with equation (51). This analysis also applies to other small bubbles. For example, at a given redshift the bubble feature produced with $d = 0.1$ Mpc calculated with $v_{\rm turb} = 100$ km s^{-1} is comparable with that produced with $d = 0.01$ Mpc calculated with $v_{\rm turb} = 10$ km s^{-1}.

The large bubbles can be approximated in a similar way. The features created by large bubbles (which satisfy ${\rm d}\nu_{\rm bubble} \gg {\rm d}\nu_\phi$) can be separated into three parts. For example, the 10 Mpc bubble feature in the middle panel of Fig. 4 starts and ends approximately at frequencies

$$\nu_{\rm begin} = (\nu_{21\rm cm} - 0.5{\rm FWHM}_\nu)/(1+z)|_{z=z_{\rm begin}} \quad (52)$$

and

$$\nu_{\rm end} = (\nu_{21\rm cm} + 0.5{\rm FWHM}_\nu)/(1+z)|_{z=z_{\rm end}}. \quad (53)$$

This feature can be approximately separated by

$$\nu_{\rm left} = (\nu_{21\,\rm cm} + 0.5{\rm FWHM}_\nu)/(1+z)|_{z=z_{\rm begin}} \quad (54)$$

and

$$\nu_{\rm right} = (\nu_{21\,\rm cm} - 0.5{\rm FWHM}_\nu)/(1+z)|_{z=z_{\rm end}} \quad (55)$$

into left, middle, and right part. The left part (from $\nu_{\rm begin}$ to $\nu_{\rm left}$) and right part (from $\nu_{\rm right}$ to $\nu_{\rm end}$) are both approximately half of a Gaussian shape and their width are approximately $0.5{\rm FWHM}_\nu/(1+z) = 0.5{\rm d}\nu_\phi$, the intensity of the middle part (from $\nu_{\rm left}$ to $\nu_{\rm right}$) is very close to 0. These estimated frequencies are of $\lesssim$0.1 MHz accuracy. For example, $\nu_{\rm left} = 109.2923$ MHz for the 10 Mpc bubble feature in Fig. 4; the bubble feature ($I_{\rm bubble} - I_{\rm nobubble}$) computed from C21LRT calculation has the (left) maximum value at 109.3358 MHz.

For bubbles of intermediate size (${\rm d}\nu_{\rm bubble} \sim {\rm d}\nu_\phi$), they produce spectral features between $\nu_{\rm left}$ and $\nu_{\rm right}$. Their spectral features are similar to a Gaussian function but cannot be fitted perfectly with a Gaussian function. This is because their spectral features are determined by the convolution between the line profile and other radiative transfer effects over a relatively wide redshift range.[5]

We note that these approximations are only valid because we adopted a constant $v_{\rm turb}$, hence a constant normalized line profile, for each calculation and all the bubbles we inserted are fully ionized. The features will be too complicated to be approximated analytically if we adopt realistic $n_{\rm H\,I}$ and $v_{\rm turb}$ values, which could have large spatial variation within one ionized cavity created by an astrophysical source.

[5]When we fit these bubble features with Gaussian function, the fitted Gaussian function is flatter than the bubble feature, i.e. the height of bubble feature $|I_{\rm max}|$ is noticeable larger than the fitted height $|A_{\rm fit}|$.

Table 1. Results of Gaussian fit analysis. We fitted the bubble feature with a Gaussian function (see main text for the details of bubble feature and the fitting processes). From left to right, the columns are, (i) turbulent velocity $v_{\rm turb}$ adopted when calculating the bubble feature for $d = 0.01$ Mpc at $z_{\rm begin} = 12.0$, (ii) fitted width at half-maximum $\mathrm{d}\nu_{\rm fit}$ of the bubble feature, (iii) adopted line profile width at half-maximum $\mathrm{d}\nu_\phi$ as determined by $v_{\rm turb}$ at $z_{\rm begin} = 12.0$, propagated to $z = 0$, (iv) difference between $\mathrm{d}\nu_\phi$ and $\mathrm{d}\nu_{\rm fit}$, (v) the maximum specific intensity (difference in intensity between the result with and without bubble) $I_{\rm max}$, (vi) the fitted height of Gaussian $A_{\rm fit}$, (vii) approximated height of the bubble feature calculated using equation (51), and (viii) relative difference between fitted Gaussian function and the calculated bubble feature averaged over from $(\nu_{\rm 21cm} - 1.5{\rm FWHM}_\nu)/(1+z)$ to $(\nu_{\rm 21cm} + 1.5{\rm FWHM}_\nu)/(1+z)$.

$v_{\rm turb}$ km s^{-1}	$\mathrm{d}\nu_{\rm fit}$ MHz	$\mathrm{d}\nu_\phi$ MHz	$\mathrm{d}\nu_\phi - \mathrm{d}\nu_{\rm fit}$ MHz	$I_{\rm max}$ erg (s cm^2 Hz sr)$^{-1}$	$A_{\rm fit}$ erg (s cm^2 Hz sr)$^{-1}$	$I_{\rm analytical}$ erg (s cm^2 Hz sr)$^{-1}$	$\bar{\delta}$ –
100	6.0696×10^{-2}	6.0686×10^{-2}	1.6087×10^{-4}	5.6694×10^{-25}	5.6681×10^{-25}	7.5315×10^{-25}	4.4682×10^{-5}
10	6.0814×10^{-3}	6.0686×10^{-3}	2.0992×10^{-3}	5.2428×10^{-24}	5.2396×10^{-24}	7.5315×10^{-24}	3.4633×10^{-4}

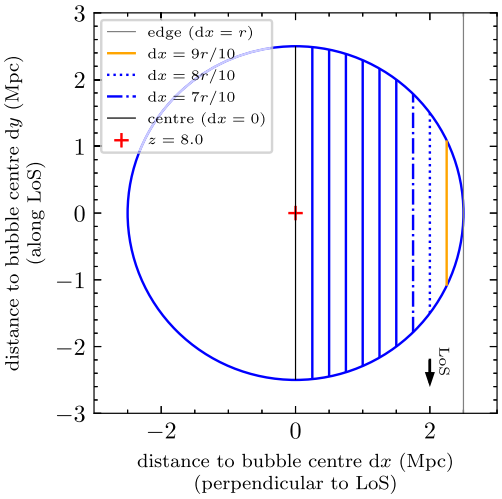

Figure 8. Using 10 rays to resolve a bubble with $r = 2.5$ Mpc at $z = 8$. The first ray is determined by the bubble centre and the observer on Earth ($\mathrm{d}x = 0$), plotted in black. All the other nine rays are parallel to the first ray, with distance $\mathrm{d}x = r/10, 2r/10, ..., 9r/10$. We use $\mathrm{d}x$ to denote distance to the first ray. The edge of the bubble is marked by the thick grey line ($\mathrm{d}x = r$), where the ray does not intersect the H II zone.

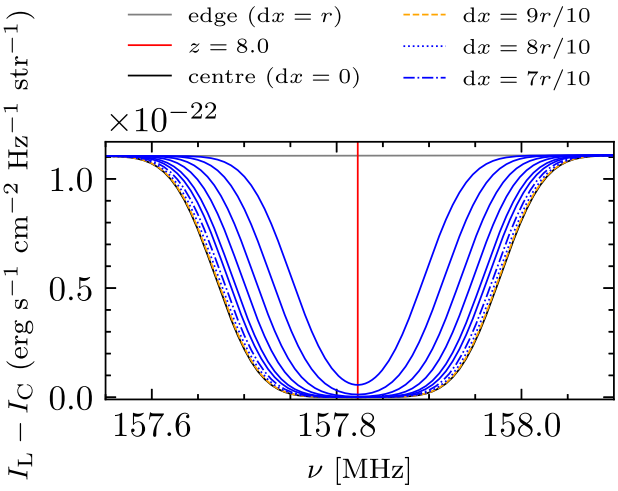

Figure 9. 21-cm spectra at $z = 0$ calculated along the 10 rays which intersect a bubble with $r = 2.5$ Mpc at $z = 8$. The 10 rays that intersect the bubble are as specified in Fig. 8.

4.1.3 Resolve a bubble with multiple rays

When ionized bubbles are large enough, it is possible to resolve each of them with multiple rays and study the changes in 21-cm features due to their spatial variations.

We used 10 rays to resolve a bubble with $d = 5.0$ Mpc ($r = 2.5$ Mpc) at $z = 8$. Different to the previous calculations, here we set the bubble centre at $z = 8$ and calculated $z_{\rm begin}$ and $z_{\rm end}$ for each ray. The bubble and the 10 rays are illustrated in Fig. 8. The first ray is determined by the bubble centre and the observer on Earth ($\mathrm{d}x = 0$), which also determines the LoS. All the other nine rays are parallel to the first ray, with distance $\mathrm{d}x = r/10, 2r/10, ..., 9r/10$. We use $\mathrm{d}x$ to denote distance to bubble centre in the perpendicular direction with respect to LoS. The edge of the bubble is marked by the thick grey line ($\mathrm{d}x = r$), where the ray does not intersect the H II bubble. We adopted a turbulent velocity of 100 km s^{-1}.[6]

The 21-cm spectra at $z = 0$ for the bubble region are shown in Fig. 9. The spectra are coded with the same colour and line styles as the corresponding rays in Fig. 8. The bubble features grows in both depth and width from $\mathrm{d}x = 9r/10$ to $\mathrm{d}x = 0$. Each bubble feature appears symmetrical to the frequency that corresponds to the bubble centre at $z = 8.0$. When $\mathrm{d}x = 9r/10$, the distance intercepted by the ray is small, and the bubble feature is still dominated by line profile width. As $\mathrm{d}x$ decreases, the intercepted distance grows and dominates over the line profile width.

So far, we have been measuring the bubble size or the intercepted distance in the rest frame of the (assumed) ionizing source at the centre of the bubbles. This is no longer accurate if the bubble is expanding with velocities v comparable with the speed of light. When v is comparable with c, the size of the bubble changes significantly within the light crossing time (e.g. of the ray which intersect the bubble centre) as discussed in Section 2.3. The apparent shape probed with 21-cm line is different from the shape observed from the local rest frame of the ionizing source. We followed Yu (2005) and calculated the apparent shape of a bubble with a constant $v = 0.9\ c$, as shown with the black ellipse in Fig. 10. Instead of assigning rays by $\mathrm{d}x = r/10, 2r/10, ...r$, we first calculate the maximum distance to the centre ray $x_{\rm max}$ and assign rays with $\mathrm{d}x = x_{\rm max}/10, 2x_{\rm max}/10, ...9x_{\rm max}/10$. We can see that due to a large v, the apparent shape significantly changed.[7] The intercepted distances decreased for all the 10 rays compared with Fig. 8. The resulting 21-cm spectra $z = 0$ are shown in Fig. 11. The rays close to the edge

[6]We note that this 100 km s^{-1} turbulent velocity may not be achieved for a realistic ionization bubble. It is chosen such that the distortion of the apparent shape of the ionization front, due to the finite speed of light, can be clearly demonstrated.

[7]The bubble is still axisymmetric with respect to the ray which intercept the bubble centre.

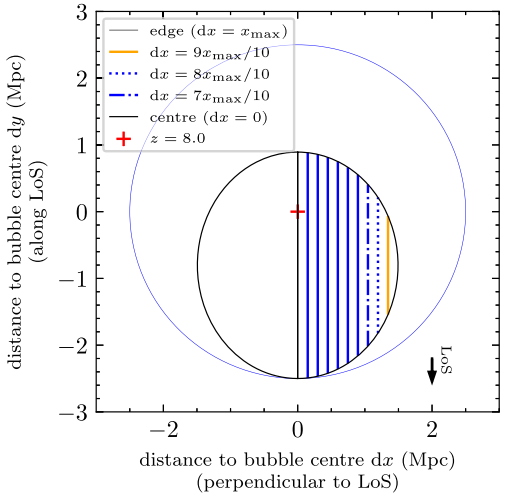

Figure 10. Using 10 rays to resolve an expanding bubble at $z = 8$ whose ionization front is expanding with a velocity of $v = 0.9\,c$ in the local rest frame of an assumed ionizing source, marked by the red cross. When the bubble has expanded to $r = 2.5$ Mpc in the rest frame (marked by the blue circle), we calculate the apparent shape due to finite speed of light (see main text for details). The apparent shape is indicated with the black ellipse. The 10 rays are equally spaced, with the first ray intercept the bubble centre ($\mathrm{d}x = 0$), plotted in black. The other nine rays have distance $\mathrm{d}x = x_{\rm max}/10, 2x_{\rm max}/10, \ldots\ldots, 9x_{\rm max}/10$. The edge of the bubble is marked by the thick grey line ($\mathrm{d}x = r$), where the ray does not intersect the H II zone.

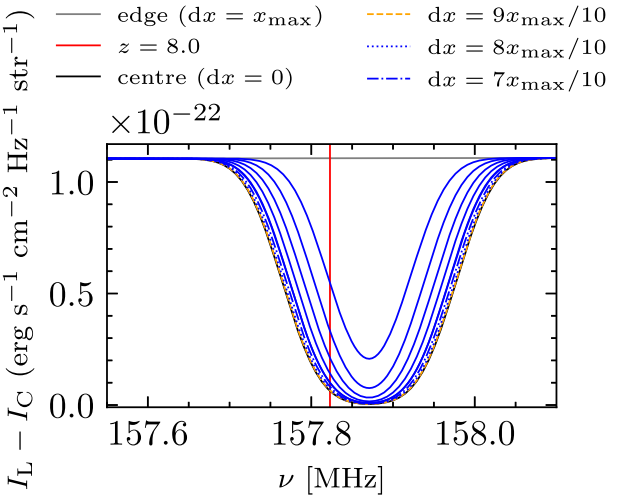

Figure 11. 21-cm spectra at $z = 0$ calculated along the 10 rays which intersect an expanding bubble with the ionization front's velocity of $v = 0.9\,c$ and an initial radius $r = 2.5$ Mpc in the local rest frame of the source at $z = 8$. The 10 rays that intersect the bubble are as specified in Fig. 10. Compared with the spectra shown in Fig. 9 for a non-locally expanding bubble, the spectral features are narrower and are no longer symmetrical with respect to the frequency marked by the red vertical line ($z = 8.0$).

of bubbles intercept much shorter distances (where there is no H I) and the width of the corresponding bubble features are dominated by line profile width. All the spectra features are narrower compared with those in Fig. 9. These spectra no longer appear symmetrical with respect to the frequency marked with red vertical line ($z = 8.0$).

4.1.4 Differences between C21LRT and optical depth parametrization

Using identical H I gas properties as inputs, the absolute difference in the spectra at $z = 0$ calculated with C21LRT and optical depth parametrization method, denoted by δ, primarily arises from two factors. First, the optical depth method tracks the signal evolution only in redshift space, while C21LRT tracks 21-cm line in a two-dimensional (redshift and frequency) space. This results in an approximate 5−10 per cent difference across all redshifts. The second factor stems from the simplifications used in deriving the optical depth parametrization, at the expense of neglecting small-scale variations of H I gas. Both factors are discussed in Chan et al. (2023). The second factor is evident when H I gas properties undergo abrupt changes, such as the transition between neutral and ionized zones. For a non-zero FWHM$_\nu$, δ reaches its maximum at approximately $\nu_{\rm left}$ and $\nu_{\rm right}$ as defined in equations (54) and (55), where $I_{\rm L} - I_{\rm C}$ immediately drops to 0 based on optical depth method, whereas $|\delta| \approx (I_{\rm L} - I_{\rm C})/2$ based on C21LRT calculations.[8] For smaller bubbles where $\mathrm{d}\nu_\phi > \mathrm{d}\nu_{\rm bubble}$, $|\delta|$ remains greater than 0 throughout the relevant frequency range (from $\nu_{\rm begin}$ to $\nu_{\rm end}$, as defined in equations 52 and 53). For larger bubbles, $|\delta|$ decreases to 0 between $\nu_{\rm left}$ and $\nu_{\rm right}$. These differences mostly result from the rest frame 21-cm broadening, with a minor contribution from radiative transfer effects.

The bubble features can also be understood as follows: For the optical depth method (with $v_{\rm turb} = 0$ implicitly assumed), the 'loss' of the 21-cm signal due the presence of an ionized bubble is distributed between $\nu_{21\rm cm}/(1+z)|_{z=z_{\rm begin}}$ and $\nu_{21\rm cm}/(1+z)|_{z=z_{\rm end}}$. For the cases presented in Figs 4–7, the value of $v_{\rm turb}$ determines the FWHM$_\nu$ (equation 50). The 'loss' of 21-cm signal is distributed over a broader frequency range between $\nu_{\rm begin}$ and $\nu_{\rm end}$. The shape of the spectral feature is determined mainly by the 21-cm line profile.

Additionally, when using the optical depth method to compute the 21-cm signals seen by a present-day observer, it often involves a separate prescription to incorporate the light from past epochs that can reach us now. This is often done by constructing a light-cone from sequential snapshots of the simulated box, where the same part of the universe has evolved with cosmological time. However, the optical depth method is inaccurate when 21-cm line is broadened or not optically thin (Chapman & Santos 2019). It can also overlook certain cosmological effects, such as the alterations in the apparent shape of the expanding ionization fronts.

4.2 Discussion

4.2.1 Implications of our results

For more sophisticated ionized cavities in cosmological simulations, their impacts on the 21-cm spectra and power spectra are currently all calculated with the optical depth parametrization. This means that the radiative processes (e.g. line broadening due to turbulent velocity) which happens on length-scales of or smaller than the sizes of the ionized cavities are missing in their calculation. When observational data become available, the sizes of ionized cavities in EoR inferred from their calculated 21-cm power spectra can have large uncertainties. For example, if ionized cavities all have sharp boundaries (the ionized fraction changes quickly from 1 to 0) and

[8]This means that, compared with the C21LRT results (considered more accurate), the signals computed from the optical depth method can have 100 per cent discrepancy near ionization fronts.

have a characteristic diameter d, the optical depth parametrization would predict a sharp change in the power spectra near $k = 1/d$, while full radiative transfer calculations would predict gradual changes near $k = 1/d$.

4.2.2 *Some remarks on the ionized cavity models*

In this work, we have used the two-zone model to show the features that it imprints on the 21-cm spectra. The two-zone model is a plausible representation of the ionized cavities carved out by the very luminous astrophysical sources when the partially ionized zone has negligible size, such as quasars.[9] The propagation of the ionizing front created by powerful ionizing sources, as captured in the expanding bubble scenario (presented in Section 4.1.3) has demonstrated that the time evolution of ionization structures needs to be corrected.

In some situations, the two-zone model may not be able to fully capture thermodynamics and geometrical properties of the ionized cavities. For instance, UV radiation from individual sources such as Population III stars or Population II stars would ionize the surrounding H I gas gradually over time. This would allow the photoionization and recombination processes to reach a quasi-equilibrium state, in which the size of the cavity would be approximately the Strömgren radius (see Strömgren 1939). In the more complicated situations, such as that the ionization source is a group of star-forming galaxies or a galaxy hosting AGNs, the radiation flux and spectrum would vary with time. The interplay between microscopic processes (such as photoionization, recombination, and radiative cooling loss) and macroscopic processes (such as hydrodynamical bulk flows) will give rise to instabilities. The distribution of H I gas near the ionizing sources is no longer uniform and smooth. The media both inside and outside the ionized cavities can be clumpy, and the 21-cm spectral signature of these cavities will be very different to those obtained from the model bubbles constructed using a globally averaged $n_{\rm H\,I}$. The development of the ionization structure created by these sources are jointly determined by the ionization, recombination processes as well as the thermodynamic processes (Axford 1961; Newman & Axford 1968; Yorke 1986; Franco et al. 2000). Transition layer of partially ionized gas can vary in thickness, ionization state, and thermodynamics properties. Furthermore, in the presence of X-ray emissions, which penetrate more deeply than UV photons and are more efficient at heating gas, ionized cavities are expected to much larger with a hazier boundary. Over time, ionized bubbles also came to overlap. All these factors are expected to individually and collectively affect the 21-cm power spectra (Finlator et al. 2012; Kaurov & Gnedin 2014; Hassan et al. 2016; Mao et al. 2020). Our future studies will look into these complex ionization structures in more detail, as C21LRT can interface with the simulated data with small-scale ($\lesssim$10 kpc) structures in the future (see Appendix A for details).

5. CONCLUSION

We investigated the 21-cm spectral features imprinted by individual spherical ionized cavities enveloped by H I medium, adopting a covariant formulation for tracking 21-cm signals in both redshift and frequency space. We studied the improvement in accuracies of the 21-cm signals, compared with adopting the optical depth parametrization, which tracks 21-cm in the redshift space only.

We use a cosmological radiative transfer code C21LRT for the numerically calculation of 21-cm signals. We showed that the evolution of ionized cavities as driven by ionization, thermodynamical, and cosmological effects, would affect the apparent shape of the cavities when probed with 21-cm line. The apparent shape of an evolving cavity is different from its shape in the rest frame of its stationary cavity centre, as there is a time lap between the radiation from the farside and from the nearside of the cavity.

We employed a set of single-ray calculations to show how the spectral features evolve with various bubble diameters d = 0.01, 0.1, 1.0, 10.0 Mpc. We found that the widths of spectral features imprinted by bubbles are jointly determined by the 21-cm FWHM$_\nu$, the bubble diameter d, and the redshift of the bubble z. The spectral feature width at redshift z can be approximated with max($\mathrm{d}\nu_\phi$, $\mathrm{d}\nu_{\rm bubble}$), where $\mathrm{d}\nu_\phi = \mathrm{FWHM}_\nu/(1+z)$ and $\mathrm{d}\nu_{\rm bubble}$ is the bubble diameter when measured in frequency space at $z = 0$.

When the 21-cm line FWHM$_\nu$ dominates ($\mathrm{d}\nu_{\rm bubble} \ll \mathrm{d}\nu_\phi$), as we adopted a Gaussian function shape 21-cm line profile, the bubble spectral feature has a Gaussian function like shape. For bubbles with smallest d in our paper (0.01 Mpc), their spectral features can be fitted with Gaussian function with negligible residuals. As d increases ($\mathrm{d}\nu_{\rm bubble} \sim \mathrm{d}\nu_\phi$), the convolution between line profile and other radiative transfer and cosmological effects becomes non-negligible and their spectral shape deviates from Gaussian functions. For these bubbles ($\mathrm{d}\nu_{\rm bubble} \lesssim \mathrm{d}\nu_\phi$), the 21-cm specific intensity $I_{\rm L} - I_{\rm C}$ does not decrease to 0 in the corresponding frequency ranges.

For large bubbles ($\mathrm{d}\nu_{\rm bubble} \gg \mathrm{d}\nu_\phi$), the widths of their spectral features are dominated by $\mathrm{d}\nu_{\rm bubble}$. These features can be divided into three parts. The shape of the left and right parts of the spectral feature is similar to half Gaussian functions. They are produced by the transition between H I and H II zone and their shape is mainly determined by the 21-cm line profile. The middle part of their spectral feature has $I_{\rm L} - I_{\rm C} = 0$. In comparison, the optical depth parametrization predicts that 21-cm signal will diminish to 0 for a fully ionized bubble, regardless of its size. We showed that the 21-cm intensities computed with it can have large discrepancies in the transition zones (ionization fronts) from those computed with C21LRT.

The 21-cm signals associated with length-scales equal to or smaller than the sizes of the ionized cavities need to be tracked in both redshift and frequency space for accuracy. For these scales, physical processes, such as line-broadening due to turbulent motion of the gas imprints on the 21-cm signals, cannot be accurately computed with the optical depth parametrization. Explicit covariant radiative transfer, such as the C21LRT, is necessary for correctly and self-consistently accounting for the convolution of local (thermodynamics and atomic processes and bubble dynamics) and global (cosmological expansion) effects onto the radiation that we receive from EoR.

ACKNOWLEDGEMENTS

We thank Richard Ellis for critically reading through the manuscript. JYHC is supported by the University of Toronto Faculty of Arts & Science Postdoctoral Fellowship with the Dunlap Institute, and the Natural Sciences and Engineering Research Council of Canada (NSERC), (funding reference #CITA 490888–16), through a CITA Fellowship. The Dunlap Institute is funded through an endowment established by the David Dunlap family and the University of

[9]We tested the three-zone model by adding a thin partially zone near the boundary (similar to the illustration in Fig. 1) and found that the features in the 21-cm spectra of the two-zone and three-zone models are actually very similar. We therefore do not show the results of three-zone models in this paper.

Toronto. QH is supported by a UCL Overseas Research Scholarship and a UK STFC Research Studentship. KW and QH acknowledge the support from the UCL Cosmoparticle Initiative. This work is supported in part by a UK STFC Consolidated Grant awarded to UCL-MSSL. This research had made use of NASA's Astrophysics Data System.

DATA AVAILABILITY

The theoretical data generated in the course of this study are available from the corresponding author QH, upon reasonable request.

REFERENCES

Axford W. I., 1961, Phil. Trans. R. Soc. A, 253, 301
Baek S., Semelin B., Di Matteo P., Revaz Y., Combes F., 2010, A&A, 523, A4
Barkana R., Loeb A., 2006, MNRAS, 372, L43
Basu A., Sur S., 2021, Galaxies, 9, 62
Bisbas T. G. et al., 2015, MNRAS, 453, 1324
Bolton J. S., Gaikwad P., Haehnelt M. G., Kim T.-S., Nasir F., Puchwein E., Viel M., Wakker B. P., 2022, MNRAS, 513, 864
Chan J. Y. H., Wu K., On A. Y. L., Barnes D. J., McEwen J. D., Kitching T. D., 2019, MNRAS, 484, 1427
Chan J. Y. H., Han Q., Wu K., McEwen J. D., 2023, MNRAS, 531, 434
Chapman E., Santos M. G., 2019, MNRAS, 490, 1255
Chardin J., Kulkarni G., Haehnelt M. G., 2018, MNRAS, 478, 1065
Datta K. K., Mellema G., Mao Y., Iliev I. T., Shapiro P. R., Ahn K., 2012, MNRAS, 424, 1877
DeBoer D. R. et al., 2017, PASP, 129, 045001
Doussot A., Semelin B., 2022, A&A, 667, A118
Eide M. B., Graziani L., Ciardi B., Feng Y., Kakiichi K., Di Matteo T., 2018, MNRAS, 476, 1174
Eide M. B., Ciardi B., Graziani L., Busch P., Feng Y., Di Matteo T., 2020, MNRAS, 498, 6083
Essen L., Donaldson R. W., Bangham M. J., Hope E. G., 1971, Nature, 229, 110
Evoli C., Ferrara A., 2011, MNRAS, 413, 2721
Fan X., Carilli C. L., Keating B., 2006, ARA&A, 44, 415
Fedchenko A. S., Krasnobaev K. V., 2018, J. Phys.: Conf. Ser., 1129, 012012
Finlator K., Oh S. P., Özel F., Davé R., 2012, MNRAS, 427, 2464
Franco J., Kurtz S. E., García-Segura G., Hofner P., 2000, Ap&SS, 272, 169
Friedrich M. M., Mellema G., Alvarez M. A., Shapiro P. R., Iliev I. T., 2011, MNRAS, 413, 1353
Fuerst S. V., Wu K., 2004, A&A, 424, 733
Furlanetto S. R., Zaldarriaga M., Hernquist L., 2004, ApJ, 613, 1
Furlanetto S. R., McQuinn M., Hernquist L., 2006a, MNRAS, 365, 115
Furlanetto S. R., Oh S. P., Briggs F. H., 2006b, Phys. Rep., 433, 181
Geil P. M., Wyithe J. S. B., 2008, MNRAS, 386, 1683
Geil P. M., Mutch S. J., Poole G. B., Duffy A. R., Mesinger A., Wyithe J. S. B., 2017, MNRAS, 472, 1324
Ghara R., Choudhury T. R., Datta K. K., Choudhuri S., 2017, MNRAS, 464, 2234
Gillet N. J. F., Aubert D., Mertens F. G., Ocvirk P., 2021, MNRAS, 507, 3179
Hassan S., Davé R., Finlator K., Santos M. G., 2016, MNRAS, 457, 1550
Hellwig H., Vessot R., Levine M., Zitzewitz P., Allan D., Glaze D., 1970, IEEE Trans. Instrum. Meas., 19, 200
HERA Collaboration, 2022, ApJ, 924, 51
Hitomi Collaboration et al., 2018, PASJ, 70, 9
Hutter A., Dayal P., Yepes G., Gottlöber S., Legrand L., Ucci G., 2021, MNRAS, 503, 3698
Iliev I. T., Mellema G., Pen U. L., Merz H., Shapiro P. R., Alvarez M. A., 2006, MNRAS, 369, 1625
Kannan R., Garaldi E., Smith A., Pakmor R., Springel V., Vogelsberger M., Hernquist L., 2022, MNRAS, 511, 4005
Kaurov A. A., Gnedin N. Y., 2014, ApJ, 787, 146
Koopmans L. et al., 2015, Proceedings of Advancing Astrophysics with the Square Kilometre Array (AASKA14), Vol. 215, Proc. Sci., Italy, p. 1
La Plante P., Battaglia N., Natarajan A., Peterson J. B., Trac H., Cen R., Loeb A., 2014, ApJ, 789, 31
Lin Y., Oh S. P., Furlanetto S. R., Sutter P. M., 2016, MNRAS, 461, 3361
Loeb A., Barkana R., 2001, ARA&A, 39, 19
Lu T.-Y., Mason C. A., Hutter A., Mesinger A., Qin Y., Stark D. P., Endsley R., 2024, MNRAS, 528, 4872
Mangena T., Hassan S., Santos M. G., 2020, MNRAS, 494, 600
Mao Y., Koda J., Shapiro P. R., Iliev I. T., Mellema G., Park H., Ahn K., Bianco M., 2020, MNRAS, 491, 1600
Mertens F. G. et al., 2020, MNRAS, 493, 1662
Mesinger A., 2016, Astrophysics and Space Science Library, Vol. 423, Understanding the Epoch of Cosmic Reionization: hallenges and Progress. Springer International Publishing, Switzerland
Mesinger A., Furlanetto S., Cen R., 2011, MNRAS, 411, 955
Morales M. F., Wyithe J. S. B., 2010, ARA&A, 48, 127
Muñoz J. B., Qin Y., Mesinger A., Murray S. G., Greig B., Mason C., 2022, MNRAS, 511, 3657
Natarajan A., Yoshida N., 2014, Prog. Theor. Exp. Phys., 2014, 06B112
Newman R. C., Axford W. I., 1968, ApJ, 153, 595
Oliva-Altamirano P., Fisher D. B., Glazebrook K., Wisnioski E., Bekiaris G., Bassett R., Obreschkow D., Abraham R., 2018, MNRAS, 474, 522
Park J., Mesinger A., Greig B., Gillet N., 2019, MNRAS, 484, 933
Parrish I. J., Quataert E., Sharma P., 2010, ApJ, 712, L194
Patrício V. et al., 2018, MNRAS, 477, 18
Peacock J. A., 1999, Cosmological Physics. Cambridge Univ. Press, Cambridge
Planck Collaboration XVI, 2014, A&A, 571, A16
Planck Collaboration XIII, 2016a, A&A, 594, A13
Planck Collaboration XLVI, 2016b, A&A, 596, A107
Planck Collaboration XLVII, 2016c, A&A, 596, A108
Pritchard J. R., Loeb A., 2012, Rep. Prog. Phys., 75, 086901
Robertson B. E., Ellis R. S., Dunlop J. S., McLure R. J., Stark D. P., 2010, Nature, 468, 49
Ruszkowski M., Oh S. P., 2011, MNRAS, 414, 1493
Santos M., Ferramacho L., Silva M., Amblard A., Cooray A., 2010, Astrophysics Source Code Library, record ascl:1010.025
Schaeffer T., Giri S. K., Schneider A., 2023, MNRAS, 526, 2942
Schmidt W., 2015, Living Rev. Comput. Astrophys., 1, 2
Schuecker P., Finoguenov A., Miniati F., Böhringer H., Briel U. G., 2004, A&A, 426, 387
Shapiro P. R., Giroux M. L., 1987, ApJ, 321, L107
Shin M.-S., Trac H., Cen R., 2008, ApJ, 681, 756
Strömgren B., 1939, ApJ, 89, 526
Subramanian K., Shukurov A., Haugen N. E. L., 2006, MNRAS, 366, 1437
Thomas R. M. et al., 2009, MNRAS, 393, 32
Tingay S. J. et al., 2013, PASA, 30, e007
Trott C. M. et al., 2020, MNRAS, 493, 4711
Vazza F., Jones T. W., Brüggen M., Brunetti G., Gheller C., Porter D., Ryu D., 2017, MNRAS, 464, 210
Weber J. A., Pauldrach A. W. A., Knogl J. S., Hoffmann T. L., 2013, A&A, 555, A35
Wright E. L., 2006, PASP, 118, 1711
Wyithe J. S. B., Loeb A., 2004, ApJ, 610, 117
Xu S., Zhang B., 2020, ApJ, 898, L48
Xu H., Wise J. H., Norman M. L., Ahn K., O'Shea B. W., 2016, ApJ, 833, 84
Yorke H. W., 1986, ARA&A, 24, 49
Younsi Z., Wu K., Fuerst S. V., 2012, A&A, 545, A13
Yu Q., 2005, ApJ, 623, 683
Zahn O., Lidz A., McQuinn M., Dutta S., Hernquist L., Zaldarriaga M., Furlanetto S. R., 2007, ApJ, 654, 12
Zarka P., Girard J. N., Tagger M., Denis L., 2012, in Boissier S., de Laverny P., Nardetto N., Samadi R., Valls-Gabaud D., Wozniak H., eds, SF2A-2012: Proceedings of the Annual meeting of the French Society of Astronomy and Astrophysics. French Astronomical Society, Paris, France, p. 687
Zhang J.-F., Wang R.-Y., 2022, Frontiers Astron. Space Sci., 9, 869370

APPENDIX A: COMPUTATIONAL TIME

In our calculations, H II bubbles are all resolved with at least 10 redshift cells. We still used a rectangular two-dimensional grid in $\log \nu$–$\log(1+z)$ space (see appendix A of Chan et al. 2023 for details). For the smallest bubbles $d = 0.01$ Mpc, their sizes when measured in redshift space are $\sim 10^{-5}$ at $z \sim 10$, hence we have already used redshift resolution of $\Delta_{\log(1+z)} \equiv \log(1+z') - \log(1+z) < 10^{-6}$. When measured with comoving distances, this shows that C21LRT can resolve scales down to $\sim$1 kpc. The best frequency resolution in this paper, when adopting the smallest turbulent velocity of 1 km s^{-1} to produce the result shown in Fig. 7, is $\Delta_{\log \nu} \equiv \log \nu_{z'} - \log \nu_z = 10^{-6}$. This shows that C21LRT can resolve small turbulent velocity $v_{\rm turb} = 10$ km s^{-1} with accuracy. In each calculation, the ray is traced from $z = z_{\rm begin} + \Delta z_1$ to $z = z_{\rm end} - \Delta z_2$, where Δz_1 and Δz_2 need to be larger than $\Delta z_1'$ and $\Delta z_2'$. Their values are determined by the effective line profile width (when translated into redshift space) as follows:

$$\frac{\nu_{\rm 21cm}}{1+z_{\rm begin}+\Delta z_1'} = \frac{\nu_{\rm 21cm} - {\rm FWHM}_\nu}{1+z_{\rm begin}}\,, \tag{A1}$$

and

$$\frac{\nu_{\rm 21cm}}{1+z_{\rm end}-\Delta z_2'} = \frac{\nu_{\rm 21cm} + {\rm FWHM}_\nu}{1+z_{\rm end}}\,. \tag{A2}$$

We adopted $\Delta z_1 = 10\Delta z_1'$ and $\Delta z_2 = 10\Delta z_2'$ in this paper to avoid artifacts.

The C21LRT calculations were done with a desktop with 8 CPU cores and the computational time of each calculation was shorter than 1 min. In principle, for any ionization structure which spans $z_{\rm begin}$ and $z_{\rm end}$, C21LRT can resolve down to arbitrarily small spatial scales with accuracy by adopting appropriate Δz_1 and Δz_2 and using multiple rays.

This paper has been typeset from a TEX/LATEX file prepared by the author.